Magnetic Resonance Imaging 62 (2019) 129–151

Contents lists available at ScienceDirect

Magnetic Resonance Imaging

journal homepage: www.elsevier.com/locate/mri

Original contribution

Brain tissue segmentation using improved kernelized rough-fuzzy C-means with spatio-contextual information from MRI

Anindya Halder, Nur Alom Talukdar*

Department of Computer Applications, School of Technology, North-Eastern Hill University, Meghalaya794002, India

ARTICLE INFO

Keywords:
Kernel
Brain MRI
Rough-fuzzy sets
Clustering
Segmentation

ABSTRACT

Segmentation of brain tissues from MRI often becomes crucial to properly investigate any region of the brain in order to detect abnormalities. However, the accurate segmentation of the brain tissues is a challenging task as the different tissue regions are usually imprecise, indiscernible, ambiguous, and overlapping. Additionally, different tissue regions are non-linearly separable. Noises and other artifacts may also present in the brain MRI. Therefore, conventional segmentation techniques may not often achieve desired accuracy.

To deal those challenges, a robust *kernelized rough fuzzy C-means clustering with spatial constraints* (KRFCMSC) is proposed in this article for brain tissue segmentation. Here, the brain tissue segmentation from MRI is considered as a clustering of pixels problem. The basic idea behind the proposed technique is the judicious integration of the fuzzy set, rough set, and kernel trick along with spatial constraints (in the form of contextual information) to increase the clustering (segmentation) performance.

The use of rough and fuzzy set theory in the clustering process handles the ambiguity, indiscernibility, vagueness and overlappingness of different brain tissue regions. While, the kernel trick increases the chance of linear separability of the complex regions which are otherwise not linearly separable in its original feature space. In order to deal the noisy pixels, here in the clustering process, the spatio-contextual information is introduced from the neighbouring pixels.

Experiments are carried out on different real and synthetic benchmark brain MRI datasets (publicly available from Brainweb, and IBSR) without and with added noise. The performance of the proposed method is compared with five other counterpart clustering based segmentation techniques and evaluated using various supervised as well as unsupervised validity indices such as, overall accuracy, precision, recall, kappa, Jaccard, dice, and kernelized Xie-Beni index. Experimental results justify the superiority and robustness of the proposed method over other state-of-the-art methods on both benchmark real life and synthetic brain MRI datasets with and without added noise. Statistical significance of the better segmentation accuracy can be confirmed from the paired *t*-test results in favour of the proposed method compared to other counterpart methods.

1. Introduction

In bio-medical engineering, imaging technology plays the vital role for diagnostics purpose. Different diagnostic tools such as X-Ray, Computer Tomography (CT), Magnetic Resonance Imaging (MRI), and Positron Emission Tomography (PET) are available [1, 2] in medical imaging technology. Out of the existing diagnostic tools, possibly MRI is one of the widely used effective diagnostic imaging techniques that can be used for early detection of changes in organs and tissues [3, 4] preciously. Brain MRI is one of the popular applications of MRI techniques which is a safe and noninvasive investigation method that uses a magnetic field and radio waves to generate detailed images of the brain and it's stems [3]. Multimodal images of tissues with a variety of contrasts on the basis of the three magnetic resonance modalities namely, T1, T2, and PD (proton density) weighted [1, 3, 5] can be produced by the Brain MRI.

The formation of human brain is very complex and its accurate segmentation is very important for the detection and identification of edema, tumors, and necrotic tissues or any other abnormalities for prescribing proper diagnosis and suitable treatment [3, 5]. In medical practices, abnormalities are tracked by clinical investigations of the anatomical structures, morphological appearances of the regions which are highly sensitive towards the specialist's (field expert's) opinion in the process of identifying tissues and different regions which can cause the difficulties in differentiating (analyzing) abnormalities. So, in order to handle those issues and to introduce relatively faster, accurate

* Corresponding author.
E-mail addresses: anindya.halder@nehu.ac.in (A. Halder), nuralom1988@gmail.com (N.A. Talukdar).

https://doi.org/10.1016/j.mri.2019.06.010
Received 8 September 2018; Received in revised form 12 June 2019; Accepted 14 June 2019

preliminary diagnosis of abnormalities (such as cancers and tumor), and also to analyze the MRI brain, the computational approaches such as machine learning [6], image processing [7], pattern recognition [6, 8] etc. are often being applied. In automated computer aided medical image analysis, segmentation is widely used in the primary stage. Even though, medical image segmentation is a challenging and difficult task due to the inherent complex nature of the images [1, 2, 5] particularly for brain (MR) images.

Various techniques have been applied for the segmentation of MRI. In broad, they can be categorized as region-growing based [9], thresholding based [10, 11], pixel classification based [12], edge detection based [13], pattern recognition/machine-learning [14-19] based etc. Well structured reviews of MRI brain segmentation techniques can be found in [20-22].

Clustering algorithms often fail in segmenting the images corrupted by noise, outliers, and other artifacts normally present in brain MRI caused by the radio-frequency coils, which leads to inefficient results mainly due to not considering the contextual (spatial) information. Brain MRI can be corrupted by a variety of noises viz., Gaussian noise [23, 24], Rician noise [25, 26], Salt and Pepper noise (Impulse noise) [27, 28], Periodic noise [29], and Uniform noise (Quantization noise) [28]. Gaussian noise, is statistical noise that follows a probability density function (PDF) which is equal to that of the normal distribution. Primary sources of gaussian noise in digital images take place at the time of acquisition. Rician noise is the signal dependent noise which is initiated due to the formation of magnitude MRI which follows a Rice distribution [25]. Salt and Pepper noise is also known as impulsive noise or Skype noise which is basically introduced because of bit errors in transmission or by analog to digital (A/D) converter errors resulting in white pixels in dark regions and black pixels in bright region [27, 28]. Basically, electromechanical or electrical interference at the time of the brain MR image acquisition process causes the periodic noise [29]. Images corrupted by this type of noise looks like a pattern repeatedly added on the surface of the MRI. When the pixels of a sensed image is quantized to a number of discrete levels (i.e., conversion from continuous to discrete values) then it causes quantization noise which follows an approximately uniform distribution [28].

Researchers around the globe working with clustering have proposed a good number of algorithms in the last decade to deal with the noise, outliers and the problems related to intensity inhomogeneity. In this context edge segmentation [30], expectation-minimization (EM) [31] for bias field correction and tissue classification, modified FCM [32], adaptive FCM [33], shadowed c-means [34] for brain MRI segmentation and bias field estimation are proposed in the literature. A review pertinent to this problem can be found in [35].

Due to overlapping nature, ambiguity, and vagueness of the human brain, traditional computational methods sometime do not meet desired accuracy in segmenting the regions of interest (ROI) from brain MRI data. Additionally, some algorithms fail because of the presence of noise, outliers, and other artifacts (generally caused by radio-frequency coils) in MRI brain data, which may lead to inaccurate outcomes mostly due to not considering the contextual (spatial) information in the segmentation procedure.

To address the afore-said issues in this article, a novel method namely improved kernelized rough fuzzy C-means algorithm with spatio-contextual information (KRFCMSC) is proposed for the segmentation of brain tissues from MRI. The proposed technique is robust in presence of outlier and noise often in brain MRI data. Also the proposed method is capable of handling the vagueness, overlappingness, ambiguity,and indiscernibility generally present in brain MRI.

Performance of the proposed algorithm is examined with variety of real as well as synthetic benchmark brain MRI datasets with and without added noise. The segmentation results obtained by the proposed method is compared with different popular clustering based image segmentation techniques using various supervised and unsupervised validity indices such as segmentation accuracy (SA), recall, precision, micro and macro averaged F_1 measures, Jaccard, dice, Kappa, and kernelized Xie-Beni index (KXBI).

The rest of the article is organized as follows. The basics of rough-fuzzy sets and kernel trick (pertinent to the proposed technique) are discussed briefly in Section 2. In Section 3, the proposed kernelized rough fuzzy C-means with spatial constraint (KRFCMSC) is presented in details. The datasets used for the simulations along with the implemented feature generation policy, followed by the details of the validity measures used in this article are described in the experimental evaluation Section 4. In Section 5, results of the experiments and their analysis are summarized. Finally, conclusions and future work are highlighted in Section 6.

2. Preliminaries

The proposed method is based on the judicious integration of the kernel trick in rough-fuzzy clustering with spatial constraint. Therefore, brief overviews of the rough, fuzzy sets, and kernel tricks are discussed briefly in this section.

2.1. Fuzzy set

Fuzzy set [36] is a generalization of classical set. It works as the way human being reason and represents in the face of uncertainty. In set theory, a data point either fully belongs to or does not belong at all to a set and therefore such set is called as crisp set. In fuzzy set, partially belongingness is allowed i.e., an element partially may belong to a set which is known as multi degrees of membership ([0, 1]). Fuzzy set deals with logic that is approximate.

A fuzzy set F of U (where, U is a finite and nonempty set) is a mapping from U into the unit interval [0,1]: μ_F: $U \rightarrow$ [0,1] where, for each pattern $\vec{x} \in U$, we call $\mu_F(\vec{x})$ the membership degree of $\vec{x}$ in F. Larger value of the membership function represents the higher degree of the membership. It means how closely an element resembles an ideal element. Membership functions can represent uncertainty by using representative functions which can transform linguistic variables into numerical calculations by selecting some parameters. Then finally fuzzy decisions can be made.

2.2. Rough set

Pawlak [37, 38] proposed the rough set which is a formal approximation of the crisp set in terms of the lower approximation ($\underline{BX}$) and upper approximation ($\bar{B}X$). Let, $Z = (U,B)$ is an approximation space, where U is the universe (a finite set) and B is a equivalence relation which satisfies the reflexive, symmetric and transitive property on universe U. For a given subset of attributes, the set of objects may be divided in equivalence classes. Let, $X \subseteq U$, it can be defined by a lower approximation ($\underline{BX}$) and an upper approximation ($\bar{B}X$) as follows:

$$\underline{BX} = \bigcup_{X_i \in X} X_i, \quad \bar{B}X = \bigcup_{X_i \cap X \neq \emptyset} X_i \tag{1}$$

lower approximation ($\underline{BX}$) represents the set of elements of U those surely belong to X and upper approximation ($\bar{B}X$) is the set of elements of U those possibly belong to X.

2.3. Kernel trick

Kernel trick [39] applies a non-linear transformation on the input data points to project those into a high dimensional feature space by replacing the inner product with an appropriate Mercer kernel [40, 41]. Thus, the concept of kernel increases the chance of linear separability of the complex regions which are otherwise not linearly separable in its original feature space.

Let, $\phi()$ be the non-linear transformation applied on the data point

to project into a higher dimensional feature space. The inner product of $\phi(\vec{x_i})$ and $\phi(\vec{y_i})$ [42] is the kernel function $\mathbb{K}(\vec{x_i}, \vec{y_i}) = \phi(\vec{x_i})^T\phi(\vec{y_i})$. The radial basis function (RBF) generally used for kernel is: $\mathbb{K}(\vec{x_i}, \vec{y_i}) = \phi(\vec{x_i})^T\phi(\vec{y_i})$ [43]

$$\mathbb{K}(\vec{x_i}, \vec{y_i}) = \exp\left(\frac{(-\sum_{i=1}^{d} |\vec{x_i} - \vec{y_i}|^a)^b}{\sigma^2}\right) \tag{2}$$

where, d represents the dimension (feature) of the data set; $a \geq 0$;$1 \leq b \leq 2$.

3. Proposed method: improved kernelized rough-fuzzy C-means with spatio-contextual information (KRFCMSC)

To tackle the issues highlighted in the Introduction section, in this article, the concept of kernel trick is integrated in rough-fuzzy clustering further modified and improved by spatial constraints (in terms of contextual information) which is supposed to produce good segmentation results particularly for the complex brain (MRI) tissue regions those are vague, overlapping, indiscernible in nature and sometimes may be corrupted with noise.

The kernel trick helps to project the data pattern (pixels) $\vec{x_k}$ and the cluster center $\vec{v_i}$ to a higher dimensional space where the chance of separation of the clusters by a linear boundary is more.

Hence, introduction of kernel trick in the FCM [10, 11] replaces the Euclidian distance with kernel distance $\mathbb{K}(\vec{x_k}, \vec{v_i})$ which leads to a kernelized fuzzy objective function J_{KFCM} as defined in Eq. (3):

$$J_{KFCM} = 2\sum_{i=1}^{C}\sum_{k=1}^{N} \mu_{ik}^m(1 - \mathbb{K}(\vec{x_k}, \vec{v_i}));$$ (3)

Therefore, the membership function (μ_{ik}) as well as the cluster centers($\vec{v_i}$) are updated respectively as follows:

$$\mu_{ik} = \frac{(1 - \mathbb{K}(\vec{x_k}, \vec{v_i}))^{\frac{1}{1-m}}}{\sum_{i=1}^{C}(1 - \mathbb{K}(\vec{x_k}, \vec{v_i}))^{\frac{1}{1-m}}}$$ (4)

$$\vec{v_i} = \frac{\sum_{k=1}^{N}\mu_{ik}^m\mathbb{K}(\vec{x_k}, \vec{v_i})\vec{x_k}}{\sum_{k=1}^{N}\mu_{ik}^m\mathbb{K}(\vec{x_k}, \vec{v_i})}$$ (5)

where, C represents total number of clusters and N represents total number of pixels; m is the fuzziness index, $1 \leq m < \infty$.

To deal the issues related to noise and artifacts, spatial contextual information has been incorporated in the clustering process (in Eq. (3)) by allowing the pixel labels to be influenced by the effect of the immediate neighbouring pixels which is supposed to yield good segmentation results.

Introducing the spatial contextual information in the method, the objective function J_{KFCM} (in Eq. (3)) can be rewritten as given in Eq. (6).

$$J_{KFCMSC} = \sum_{i=1}^{C}\sum_{k=1}^{N} \mu_{ik}^m(1 - \mathbb{K}(\vec{x_k}, \vec{v_i})) + \alpha\sum_{i=1}^{C}\sum_{k=1}^{N} \mu_{ik}^m(1 - \mathbb{K}(\underset{\sim}{\vec{x}}_k, \vec{v_i})).$$ (6)

where, $\underset{\sim}{\vec{x}}_k$ represents the mean or median of the immediate neighbouring pixels (present in a small window typically of size 3×3 or 5×5) around the pixel $\vec{x_k}$. Unlike [32], $\underset{\sim}{\vec{x}}_k$ can be computed in advance by adopting the mean filtering or median filtering technique (here in the present work we have used the mean value for $\underset{\sim}{\vec{x}}_k$); α is a controlling parameter, that controls the effect of the neighbouring term. When the value of α equals to 0 or α approaches to ∞ (infinity) the method behaves like standard KFCM.

Theorem 1. *Optimizing the objective function J_{KFCMSC} (of Eq. (6)) with respect to membership function (μ_{ik}) and cluster center ($\vec{v_i}$) and equating them to zero subject to the constraint $\sum_{i=1}^{C}\mu_{ik} = 1$ we get the two necessary and sufficient conditions of the membership function (μ_{ik}) and cluster center ($\vec{v_i}$) for the objective function to be locally minimum respectively as follows:*

$$\mu_{ik} = \frac{((1 - \mathbb{K}(\vec{x_k}, \vec{v_i})) + \alpha(1 - \mathbb{K}(\underset{\sim}{\vec{x}}_k, \vec{v_i})))^{\frac{1}{1-m}}}{\sum_{i=1}^{C}((1 - \mathbb{K}(\vec{x_k}, \vec{v_i})) + \alpha(1 - \mathbb{K}(\underset{\sim}{\vec{x}}_k, \vec{v_i})))^{\frac{1}{1-m}}}$$ (7)

and

$$\vec{v_i} = \frac{\sum_{k=1}^{N}\mu_{ik}^m((1 - \mathbb{K}(\vec{x_k}, \vec{v_i}))\vec{x_k} + \alpha(1 - \mathbb{K}(\underset{\sim}{\vec{x}}_k, \vec{v_i}))\underset{\sim}{\vec{x}}_k)}{\sum_{k=1}^{N}\mu_{ik}^m((1 - \mathbb{K}(\vec{x_k}, \vec{v_i})) + \alpha(1 - \mathbb{K}(\underset{\sim}{\vec{x}}_k, \vec{v_i})))}$$ (8)

Proof. The optimization of the objective function J_{KFCMSC} (in Eq. (6)) under the constraint $\sum_{i=1}^{C}\mu_{ik} = 1$ can be solved by using the Lagrange multiplier technique. Therefore, in presence of Lagrange multiplier the objective function can be rewritten as follows:

$$L_{KFCMSC} = \sum_{i=1}^{C}\sum_{k=1}^{N} \mu_{ik}^m(1 - \mathbb{K}(\vec{x_k}, \vec{v_i})) + \alpha\sum_{i=1}^{C}\sum_{k=1}^{N} \mu_{ik}^m(1 - \mathbb{K}(\underset{\sim}{\vec{x}}_k, \vec{v_i})) + \sum_{k=1}^{N}\lambda_k\left(1 - \sum_{i=1}^{C}\mu_{ik}\right)$$ (9)

where, λ_k is represents the Lagrange multiplier.

Therefore, optimization of Eq. (6) is equivalent to optimizing Eq. (9). Taking the partial derivative of L_{KFCMSC} (Eq. (9)) with respect to membership function (μ_{ik}) and λ_k (Lagrange multiplier) and equating to 0 we get:

$$\begin{aligned}\frac{\partial L_{KFCMSC}}{\partial \mu_{ik}} &= 0\\ &\Rightarrow m\mu_{ik}^{m-1}(1 - \mathbb{K}(\vec{x_k}, \vec{v_i})) + \alpha m\mu_{ik}^{m-1}(1 - \mathbb{K}(\underset{\sim}{\vec{x}}_k, \vec{v_i})) - \lambda_k\\ &= 0\end{aligned}$$ (10)

$$\begin{aligned}&\Rightarrow m\mu_{ik}^{m-1}((1 - \mathbb{K}(\vec{x_k}, \vec{v_i})) + \alpha(1 - \mathbb{K}(\underset{\sim}{\vec{x}}_k, \vec{v_i}))) = \lambda_k\\ &\Rightarrow \mu_{ik} = \left(\frac{\lambda_k}{m((1 - \mathbb{K}(\vec{x_k}, \vec{v_i})) + \alpha(1 - \mathbb{K}(\underset{\sim}{\vec{x}}_k - \vec{v_i})))}\right)^{\frac{1}{m-1}}\\ &\Rightarrow \mu_{ik} = \left(\frac{\lambda_k}{m}\right)^{\frac{1}{m-1}}\left(\frac{1}{(1 - \mathbb{K}(\vec{x_k}, \vec{v_i})) + \alpha(1 - \mathbb{K}(\underset{\sim}{\vec{x}}_k, \vec{v_i}))}\right)^{\frac{1}{m-1}}\end{aligned}$$ (11)

and $\frac{\partial L_{KFCMSC}}{\partial \lambda_k} = 0$

$$\Rightarrow \sum_{i=1}^{C}\mu_{ik} = 1$$ (12)

Substituting Eq. (11) into Eq. (12) we get:

$$\sum_{i=1}^{C}\left(\frac{\lambda_k}{m}\right)^{\frac{1}{m-1}}\left(\frac{1}{(1 - \mathbb{K}(\vec{x_k}, \vec{v_i})) + \alpha(1 - \mathbb{K}(\underset{\sim}{\vec{x}}_k, \vec{v_i}))}\right)^{\frac{1}{m-1}} = 1$$

$$\Rightarrow \left(\frac{\lambda_k}{m}\right)^{\frac{1}{m-1}} = \frac{1}{\sum_{i=1}^{C}\left(\frac{1}{(1 - \mathbb{K}(\vec{x_k}, \vec{v_i})) + \alpha(1 - \mathbb{K}(\underset{\sim}{\vec{x}}_k, \vec{v_i}))}\right)^{\frac{1}{m-1}}}$$ (13)

Finally, replacing Eq. (11) by Eq. (13) we get:

Table 1
Summary of the average experimental results (of 10 simulations) obtained by the proposed KRFCMSC method and other compared methods FCM, FCMSC, RFCM, KRFCM, and KSSCM performed on various BrainWeb brain MRI datasets.

MRI data	Method	SA	Precision	Recall	Macro F_1	Micro F_1	Kappa
Z85	KRFCMSC	**94.216**	**0.922**	0.889	0.900	**0.910**	**0.910**
	FCM	85.889	0.831	0.846	0.849	0.839	0.827
	FCMSC	90.945	0.894	0.889	0.887	0.900	0.896
	RFCM	90.237	0.895	0.885	0.872	0.950	0.882
	KRFCM	91.341	0.902	**0.899**	**90.132**	0.908	0.891
	KSSCM	93.601	0.919	0.89	90.132	0.900	0.901
Z93	KRFCMSC	**94.722**	**0.925**	**0.928**	**0.926**	**0.931**	**0.911**
	FCM	88.320	0.872	0.864	0.873	0.873	0.867
	FCMSC	91.197	0.904	0.899	0.901	0.897	0.894
	RFCM	90.354	0.880	0.892	0.886	0.878	0.886
	KRFCM	92.014	0.903	0.914	0.909	0.91	0.906
	KSSCM	94.201	0.918	0.920	0.922	0.927	0.908
Z96	KRFCMSC	**95.165**	**0.929**	**0.919**	**0.916**	**0.924**	**0.939**
	FCM	89.209	0.880	0.879	0.874	0.875	0.870
	FCMSC	91.200	0.903	0.899	0.897	0.898	0.893
	RFCM	90.537	0.896	0.890	0.887	0.890	0.884
	KRFCM	91.917	0.901	0.906	0.91	0.915	0.9
	KSSCM	94.617	0.921	0.913	0.912	0.92	0.932
Z100	KRFCMSC	94.288	0.912	0.913	**0.902**	0.913	**0.917**
	FCM	87.984	0.862	0.858	0.858	0.860	0.868
	FCMSC	91.009	0.897	0.889	0.890	0.893	0.870
	RFCM	88.891	0.869	0.878	0.869	0.863	0.869
	KRFCM	90.281	0.882	0.89	0.882	0.887	0.893
	KSSCM	**94.61**	**0.915**	**0.917**	0.90	**0.909**	0.914

Table 2
Summary of the average experimental results (of 10 simulations) obtained by the proposed method KRFCMSC and other compared methods FCM, FCMSC, RFCM, KRFCM, and KSSCM performed on various IBSR brain MRI datasets.

MRI data	Method	SA	Precision	Recall	Jaccard	Dice
IBSR144	KRFCMSC	**91.346**	**0.863**	**0.789**	**0.913**	**0.954**
	FCM	86.701	0.801	0.744	0.867	0.928
	FCMSC	90.933	0.852	0.787	0.909	0.952
	RFCM	91.168	0.857	0.785	0.911	0.953
	KRFCM	89.755	0.836	0.765	0.897	0.946
	KSSCM	91.077	0.859	0.776	0.907	0.948
IBSR150	KRFCMSC	**92.829**	0.819	0.790	**0.936**	**0.971**
	FCM	91.171	0.859	0.778	0.911	0.953
	FCMSC	92.407	0.878	0.808	0.924	0.960
	RFCM	92.579	0.869	0.795	0.925	0.961
	KRFCM	91.531	0.843	0.78	0.915	0.955
	KSSCM	92.132	**0.82**	**0.793**	0.925	0.966
IBSR155	KRFCMSC	95.129	0.876	0.819	0.951	0.975
	FCM	92.201	0.778	0.757	0.922	0.959
	FCMSC	95.385	**0.902**	0.842	0.953	0.976
	RFCM	94.497	0.876	0.804	0.944	0.971
	KRFCM	94.201	0.793	0.772	0.941	0.977
	KSSCM	**95.42**	0.90	**0.846**	**0.958**	**0.978**
IBSR167	KRFCMSC	**95.407**	**0.924**	**0.843**	**0.954**	**0.976**
	FCM	92.565	0.872	0.784	0.925	0.961
	FCMSC	95.107	0.918	0.857	0.951	0.977
	RFCM	94.949	0.908	0.807	0.949	0.974
	KRFCM	94.627	0.883	0.784	0.936	0.967
	KSSCM	94.976	0.919	0.84	0.949	0.97

$$\mu_{ik} = \frac{((1 - \mathbb{K}(\vec{x_k}, \vec{v_i})) + \alpha(1 - \mathbb{K}(\underset{\sim}{\vec{x_k}}, \vec{v_i})))^{\frac{1}{1-m}}}{\sum_{i=1}^{C}((1 - \mathbb{K}(\vec{x_k}, \vec{v_i})) + \alpha(1 - \mathbb{K}(\underset{\sim}{\vec{x_k}}, \vec{v_i})))^{\frac{1}{1-m}}}.$$

Similarly, taking the partial derivative of L_{KFCMSC} with respect to cluster center ($\vec{v_i}$) and equating to zero we get:

$$\frac{\partial L_{KFCMSC}}{\partial \vec{v_i}} = 0$$

$$\Rightarrow \sum_{k=1}^{N} \mu_{ik}^{m}(1 - \mathbb{K}(\vec{x_k}, \vec{v_i}))(\vec{x_k} - \vec{v_i})(-1)$$

$$+ \alpha \sum_{k=1}^{N} \mu_{ik}^{m}(1 - \mathbb{K}(\underset{\sim}{\vec{x}}_k, \vec{v_i}))(\underset{\sim}{\vec{x}}_k - \vec{v_i})(-1) = 0$$

$$\Rightarrow \sum_{k=1}^{N} \mu_{ik}^{m}((1 - \mathbb{K}(\vec{x_k}, \vec{v_i}))(\vec{x_k}) + \alpha(1 - \mathbb{K}(\underset{\sim}{\vec{x}}_k, \vec{v_i}))\underset{\sim}{\vec{x_k}})$$

$$= \sum_{k=1}^{N} \mu_{ik}^{m}((1 - \mathbb{K}(\vec{x_k}, \vec{v_i})) + \alpha(1 - \mathbb{K}(\underset{\sim}{\vec{x}}_k, \vec{v_i})))\vec{v_i}$$

$$\Rightarrow \vec{v_i} = \frac{\sum_{k=1}^{N} \mu_{ik}^{m}((1 - \mathbb{K}(\vec{x_k}, \vec{v_i}))\vec{x_k} + \alpha(1 - \mathbb{K}(\underset{\sim}{\vec{x}}_k, \vec{v_i}))\underset{\sim}{\vec{x_k}})}{\sum_{k=1}^{N} \mu_{ik}^{m}((1 - \mathbb{K}(\vec{x_k}, \vec{v_i})) + \alpha(1 - \mathbb{K}(\underset{\sim}{\vec{x}}_k, \vec{v_i})))}.$$

This completes the proof.

To handle the indiscernibility, vagueness, uncertainty, and incompleteness of the different brain tissue regions, the rough set concept is adopted into the fuzzy set (in the objective function in Eq. (6)) which considers the fuzzy clusters as rough clusters $X_i(\forall i = 1 \text{ to } C)$ and defined by lower (BX_i) and upper ($\bar{B}X_i$) approximations. Assignment of a pixel in ($\bar{B}X_i$) and (BX_i) of rough equivalence cluster X_i (based on the fuzzy membership) is done as follows.

(1) A pixel $\vec{x_k}$ lies in at most one lower approximation BX_i of a generic rough cluster X_i.
(2) If a pixel $\vec{x_k}$ belongs to a BX_i of a rough cluster X_i, then it must also belong to $\bar{B}X_i$ of the same cluster. But, reverse may not be true always.
(3) If a pixel $\vec{x_k}$ is not a part of any BX_i of rough clusters then it belongs to $\bar{B}X_i$ of multiple rough clusters.

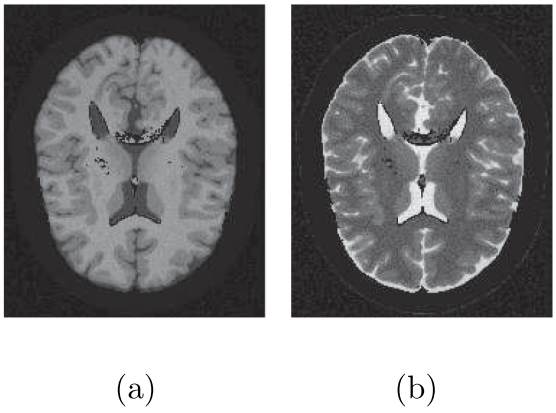

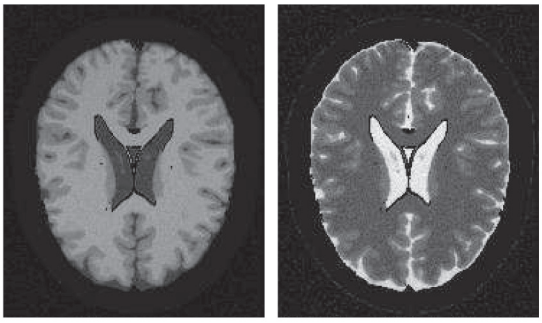

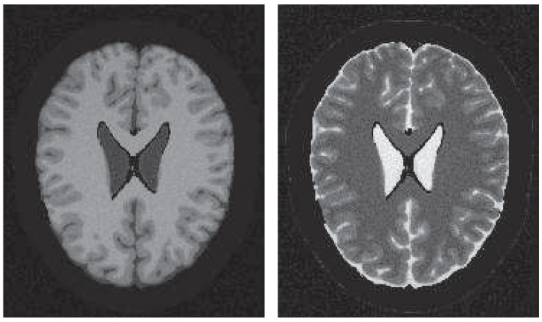

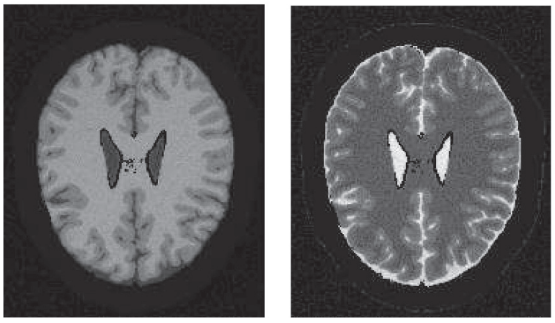

Fig. 1. First row ((a) T1-weighted (b) T2-weighted images) represents the brain MRI in Z85 plane. Second row ((c) T1-weighted (d) T2-weighted images) represents the brain MRI in Z93 plane. Third row ((e) T1-weighted (f) T2-weighted images) represents the brain MRI in Z96 plane. Fourth row ((g) T1-weighted (h) T2-weighted images) represents the brain MRI in Z100 plane.

Based on the above said characteristics, the integration of rough set concept into Eq. (6) allows us to combine fuzzy membership degree μ_{ik} of a pixel $\vec{x_k}$ to a cluster center $\vec{v_i}$, relative to all other centers $\vec{v_j}$ $\forall\, j \neq i$ (instead of the absolute individual distance d_{ik} from the centroid). This type of relative distance measure improves the clustering efficiency in presence of overlapping regions present in the image. From the condition of rough set a pixel either belongs to lower approximation of a single cluster or it belongs to upper approximations of more than one clusters as follows. If the maximum membership value of a pixel $\vec{x_k}$ for belonging to pth cluster, and $\mu_{jk}/\mu_{pk}(\forall j \neq p)$ exceeds a certain predefined *threshold* value (within the range [0.5,1]), then $\vec{x_k}$ is assigned to the upper approximation of both pth and jth clusters. Else if $\vec{x_k}$ does not lie in any upper approximation then it surely lies in the lower approximation of the pth cluster and in turn that pixel $\vec{x_k}$ also lies in the upper approximation of the pth cluster.

By incorporating the rough set, the method expects to have the following three different generic clusters (X_i), where pixels may lie:

(i) in both $\underline{BX_i}$ and $\bar{B}X_i$, which is defined by $\underline{BX_i} \neq \varnothing \wedge \bar{B}X_i - \underline{BX_i} \neq \varnothing$ in Eq. (14);
(ii) in $\bar{B}X_i$ only, that may be named as the boundary region and expressed by $\underline{BX_i} = \varnothing \wedge \bar{B}X_i - \underline{BX_i} \neq \varnothing$ in Eq. (14);
(iii) in $\underline{BX_i}$ only, which is represented by the otherwise case in Eq. (14).

Therefore, the amalgamation of rough set into kernel induced fuzzy c-means with spatial constraint requires some modifications in Eq. (6) and in Eq. (8) for the updations of the cluster centers ($\vec{v_i}$), which can be rewritten as given in Eq. (14).

$$\vec{v_i} = \begin{cases} w_{low}\dfrac{\sum_{\vec{x_k}\in \underline{BX_i}} \mu_{ik}^m (\mathbb{K}(\vec{x_k},\vec{v_i})\vec{x_k} + \alpha \underset{\sim}{\mathbb{K}}(\vec{x_k},\vec{v_i})\vec{x_k})}{\sum_{\vec{x_k}\in \underline{BX_i}} \mu_{ik}^m (\mathbb{K}(\vec{x_k},\vec{v_i}) + \alpha \underset{\sim}{\mathbb{K}}(\vec{x_k},\vec{v_i}))} + w_{up} \\ \dfrac{\sum_{\vec{x_k}\in \bar{B}X_i - \underline{BX_i}} \mu_{ik}^m (\mathbb{K}(\vec{x_k},\vec{v_i})\vec{x_k} + \alpha \underset{\sim}{\mathbb{K}}(\vec{x_k},\vec{v_i})\vec{x_k})}{\sum_{\vec{x_k}\in \bar{B}X_i - \underline{BX_i}} \mu_{ik}^m (\mathbb{K}(\vec{x_k},\vec{v_i}) + \alpha \underset{\sim}{\mathbb{K}}(\vec{x_k},\vec{v_i}))} \\ \qquad\qquad if \quad \underline{BX_i} \neq \varnothing \wedge \bar{B}X_i - \underline{BX_i} \neq \varnothing; \\ \dfrac{\sum_{\vec{x_k}\in \bar{B}X_i - \underline{BX_i}} \mu_{ik}^m (\mathbb{K}(\vec{x_k},\vec{v_i})\vec{x_k} + \alpha \underset{\sim}{\mathbb{K}}(\vec{x_k},\vec{v_i})\vec{x_k})}{\sum_{\vec{x_k}\in \bar{B}X_i - \underline{BX_i}} \mu_{ik}^m (\mathbb{K}(\vec{x_k},\vec{v_i}) + \alpha \underset{\sim}{\mathbb{K}}(\vec{x_k},\vec{v_i}))} \qquad if \quad \underline{BX_i} \\ = \varnothing \wedge \bar{B}X_i - \underline{BX_i} \neq \varnothing; \\ \dfrac{\sum_{\vec{x_k}\in \underline{BX_i}} \mu_{ik}^m (\mathbb{K}(\vec{x_k},\vec{v_i})\vec{x_k} + \alpha \underset{\sim}{\mathbb{K}}(\vec{x_k},\vec{v_i})\vec{x_k})}{\sum_{\vec{x_k}\in \underline{BX_i}} \mu_{ik}^m (\mathbb{K}(\vec{x_k},\vec{v_i}) + \alpha \underset{\sim}{\mathbb{K}}(\vec{x_k},\vec{v_i}))} \qquad otherwise \end{cases} \tag{14}$$

where, w_{up} and w_{low} are control parameters to assign weights for pixels belonging to $\underline{BX_i}$ and $\bar{B}X_i$. Generally, $w_{low} + w_{up} = 1$ and $w_{low} \in [0.5,1]$ has higher weight than w_{up}.

The complete procedure of the proposed kernelized rough fuzzy c-means with spatial constraint (KRFCMSC) is summarized in Algorithm 1.

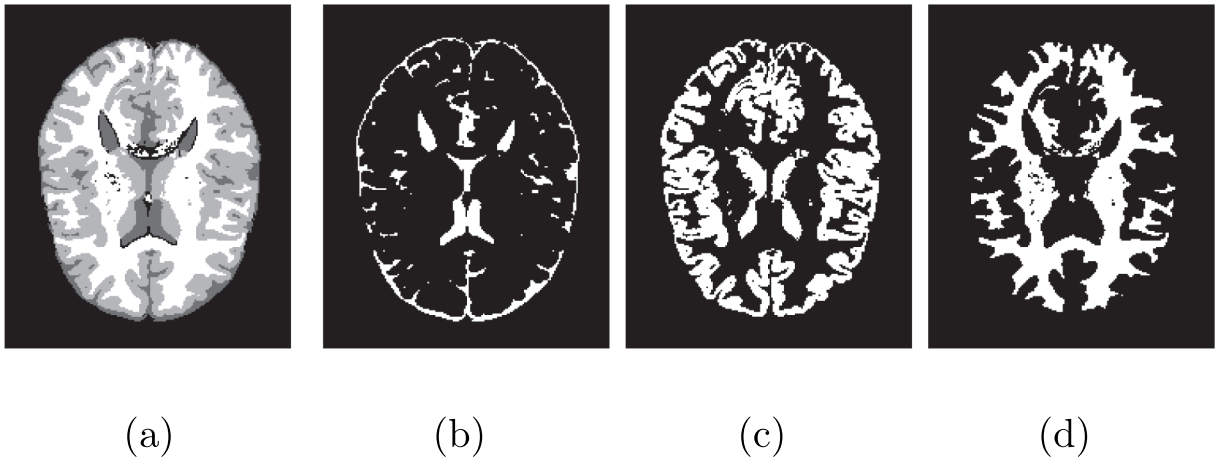

Fig. 2. Brain MRI Z85 plane: overall and individual ground truths of different segments; (a) overall ground truth, (b) CSF, (c) GM and (d) WM.

Algorithm 1. Improved kernelized rough-fuzzy C-means with spatio-contextual information.

Algorithm 1 : Improved Kernelized Rough-Fuzzy C-Means with Spatio-Contextual Information

Input: Set of pixels $\vec{x}_k$ present in the image, number of clusters C, and user defined parameters $(m, \alpha, threshold,$ and w_{low}).

Output: Set of segmented pixels (in the form segmented image).

Method:

Mean vector $\vec{\mathcal{X}}_k$ $(\forall k)$ is computed in advance for the neighbouring pixels within a small window centering around $\vec{x}_k$.
Cluster centers $\vec{v}_i, \forall i = 1\ to\ C$ are assigned randomly in the initial stage.
while (not convergence) **do**
  Memberships μ_{ik} is computed by using Equation (7) for all clusters C and all pixels N.
  for each pixel $\vec{x}_k, k = 1 : N$ **do**
    Assign the maximum membership grade for pixel $\vec{x}_k$ as follows:
    $\mu_{pk} \leftarrow \max_{j=1:C}(\mu_{jk})$,
    where, $p = \arg\max_{j=1:C}(\mu_{jk})$
    for $j = 1 : C$ and $j \neq p$ **do**
      if $\mu_{jk}/\mu_{pk} > threshold$ **then**
        $\vec{x}_k$ is assigned to the upper approximations $\overline{B}X_j$ and $\overline{B}X_p$.
      end if
    end for
    if $\vec{x}_k \notin$ any upper approximation **then**
      $\vec{x}_k$ is assigned to the lower approximation $\underline{B}X_p$.
    end if
  end for
  Cluster centers $\vec{v}_i, \forall i = 1 : C$ are updated based on Equation (14).
end while

3.1. Convergence of the proposed method

As the proposed MRI segmentation technique is based on partitive clustering process, so the process of assigning pixels to the possible clusters is repeated iteratively until convergence. The process of (re) assignment of pixels continues until there is significant changes in the cluster centers in between two consecutive iterations i.e., the clustering process converges when there is no more (re)assignment of the pixels.

The convergence of the proposed algorithm can be done by Gauss-Seidel algorithm [44] as established in [45, 46]. The Gauss-Seidel algorithm, represents a set of equations in confusion matrix (CM) form, and it is said to be converged when all the equations in the matrix is diagonally dominant. In each iteration of the algorithm, a confusion matrix $M_{c\times c}$ of the dimension $C \times C$ (where C is the clusters number) can be formed on the basis of the assigned pixels in the clustering process. When the CM is diagonally dominant then the clustering method is said to be converged, otherwise the method may or may not converge. When the cardinality of the diagonal elements in each row is

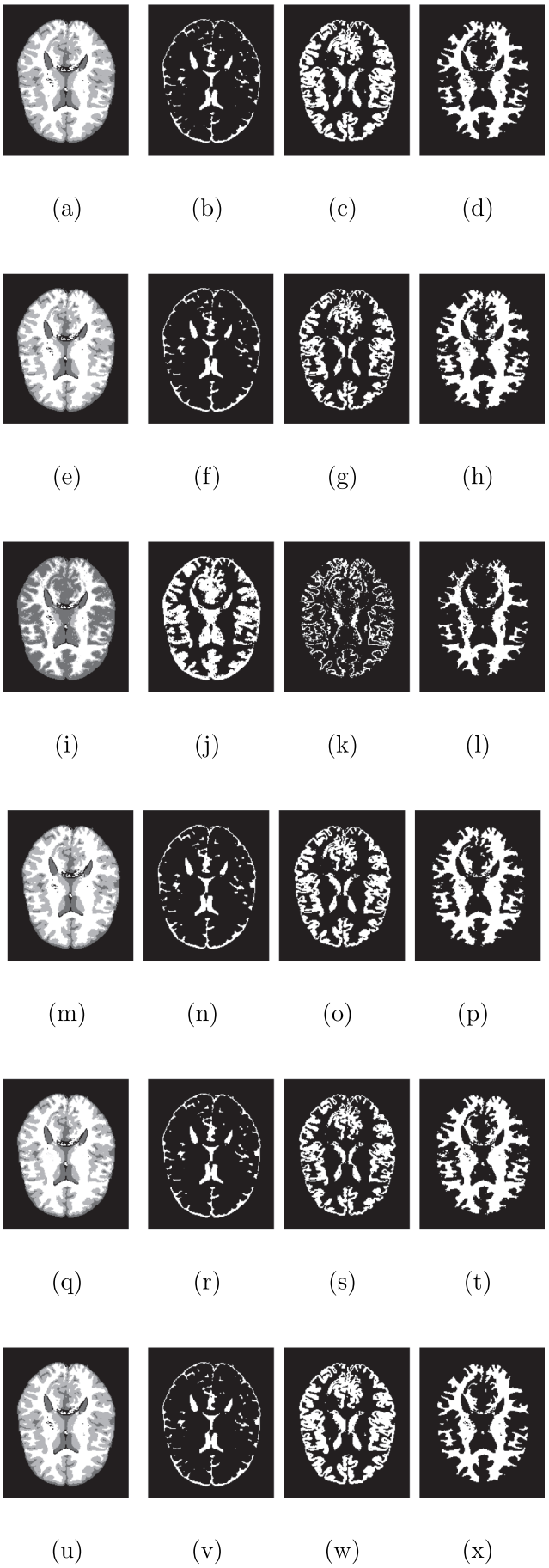

Fig. 3. Brain MRI Z85 plane: First row ((a) overall segmented image, individual segmented images of different segments viz., (b) CSF, (c) GM and (d) WM) obtained by the proposed KRFCMSC. Second row by KRFCM. Third row by FCM. Fourth row by FCMSC. Fifth row by RFCM. Sixth row by KSSCM.

greater than zero and the cardinality of the off-diagonal elements is zero or less than that of the diagonal elements in that row, then diagonal elements in each row of the CM are dominant and the method is assured to converge [44].

4. Experimental evaluation

4.1. MRI datasets used

Experiments are carried out on a variety of real as well as synthetic benchmark brain MRI datasets with and without added noise from BrainWeb image database [47] (freely available online at: http://brainweb.bic.mni.mcgill.ca/brainweb/) as well as from IBSR image database [48] (freely available online at: https://www.nitrc.org/projects/ibsr/). Where the BrainWeb dataset is synthetic in nature and IBSR dataset is real life data. The number of clusters for each MRI brain scan is considered to be four (4) namely, Gray Matter (GM), White Matter (WM), Cerebrospinal Fluid (CSF), and Background (BG) considering the significance of the major brain regions. The dimension of the images in BrainWeb dataset is (217 × 181) whereas, the size of the IBSR image is (128 × 256).

4.2. Feature generation policy

In the present investigation the pattern vector $\vec{x_k}\ \forall\ k$ or pixel (data) is formed by the T1-weighted and T2-weighted modalities of the corresponding intensity value of the pixel in the MRI brain data for the BrainWeb dataset and for the IBSR datasets only T1-weighted image is considered. It is worth noting that other features like, texture, shape etc. generated from the image may also be considered for the purpose.

4.3. Methods compared

The proposed method KRFCMSC is a clustering based segmentation technique for brain tissue segmentation from MRI. So, the performances of the proposed algorithm is compared with five widely used popular clustering based segmentation algorithms such as, (i) Fuzzy C-means (FCM) [49, 50], (ii) Rough fuzzy C-means (RFCM) [4, 51], (iii) Fuzzy C-means with Spatial constraints (FCMSC) [32], (iv) Kernelized Rough fuzzy C-means (KRFCM) [42, 52], and (v) Kernel Spatial Shadowed C-means (KSSCM) [53].

4.4. Validity indices used

The performance of the proposed algorithm is evaluated using various types of supervised and unsupervised performance measures such as (i) Segmentation accuracy (SA) [17], (ii) recall [54], (iii) precision [54], (iv) micro averaged F_1 measure [55], (v) macro averaged F_1 measure [55], (vi) Jaccard coefficient [17], (vii) Kappa [55], (viii) Dice coefficient [17], and (ix) kernelized Xie-Beni index (KXBI) [56].

- **Segmentation accuracy (SA):** Segmentation accuracy [17] is the ratio of pixels correctly identified out of the total pixels. i.e.,

$$SA = \frac{A}{B}; \tag{15}$$

  where, A is the pixels correctly identified, and B is the total pixels.
- **Precision:** Precision [54] is the ratio of pixels correctly identified (into cluster i to the total pixels identified into cluster i) i.e.,

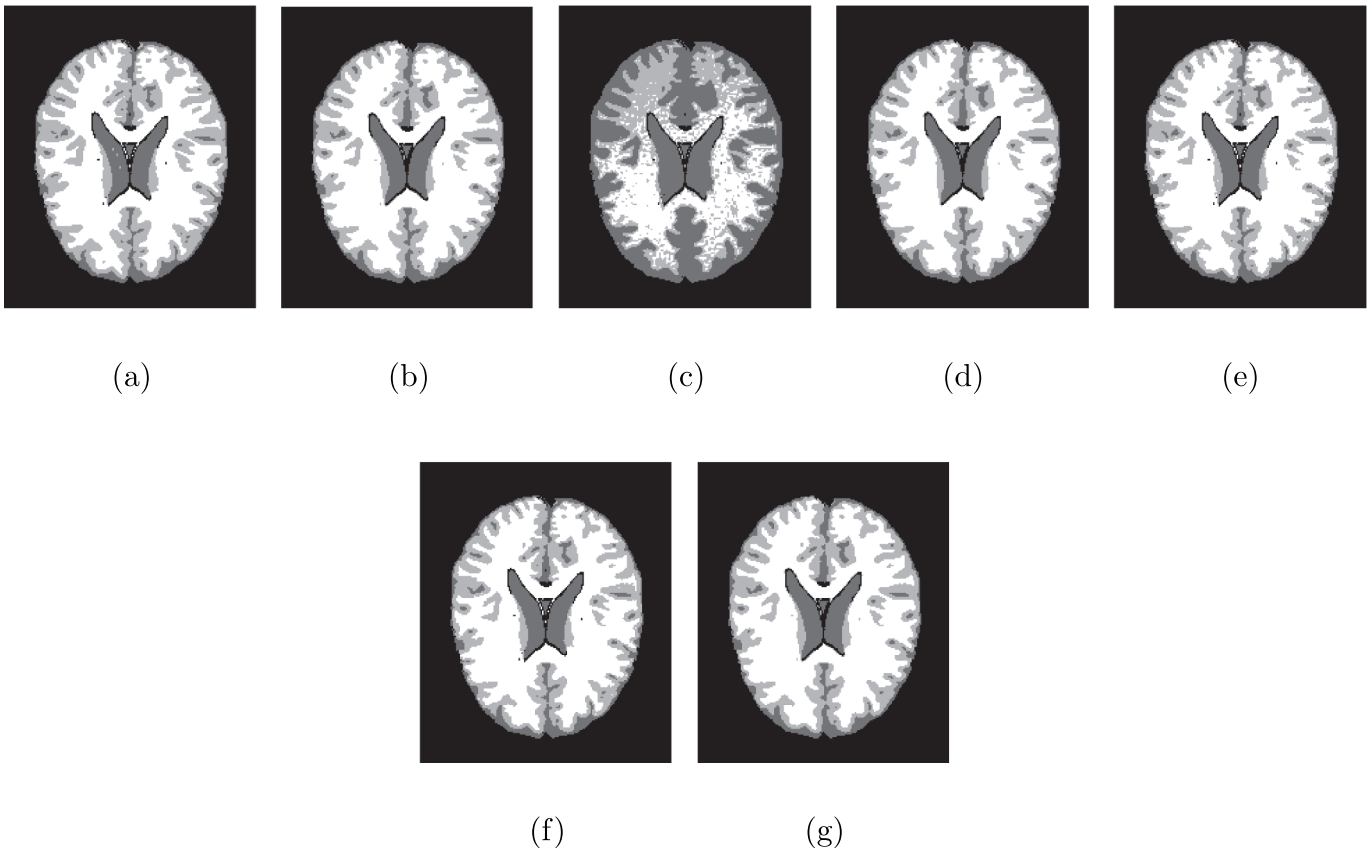

Fig. 4. Brain MRI Z93 plane: (a) Ground truth; and its segmented images obtained by: (b) proposed KRFCMSC, (c) FCM, (d) FCMSC, (e) RFCM, (f) KRFCM, and (g) KSSCM methods.

$$Precision_i(p_i) = \frac{P}{Q}; \tag{16}$$

$$Averaged \quad Precision = \frac{1}{C}\sum_{i=1}^{C} p_i. \tag{17}$$

where, C is the number of cluster present, P is the pixels correctly identified into segment i, and Q is the total number of pixels identified into segment i. Higher value indicates the better accuracy.

- **Recall:** Recall [54] is the ratio of pixels correctly identified into cluster i to the total pixels that are truly present in cluster i. i.e.,

$$Recall_i(r_i) = \frac{R}{S}; \tag{18}$$

$$Averaged \quad Recall = \frac{1}{C}\sum_{i=1}^{C} r_i. \tag{19}$$

where, C is the number of clusters, R is the pixels correctly identified into segment i, and S is the pixels that are truly present in segment i. Higher is the value of the recall better is the performance.

- **Macro averaged F_1 measure:** Macro averaged F_1 [55] measure can be derived from precision and recall. F_1, is the harmonic mean of precision and recall, of cluster i. i.e.,

$$(F_1)_i = \frac{2 \times p_i \times r_i}{p_i + r_i}. \tag{20}$$

The macro averaged F_1 measure is calculated by first calculating the F_1 scores for individual cluster and then taking mean of these per cluster scores to calculate the global mean. Macro averaged F_1 measure can be expressed as:

$$Macro \quad Averaged \quad F_1 = \frac{1}{C}\sum_{i=1}^{C} (F_1)_i; \tag{21}$$

where, C represents the cluster number. Macro averaged F_1 gives equal weight to each cluster. The value of macro averaged F_1 lies between 0 and 1. The value of the macro averaged F_1 more close to 1, better is the clustering.

- **Micro averaged F_1 measure:** Micro averaged F_1 [55] measure is computed by first creating a global contingency table whose cell values are the sum of the corresponding cells in the per-class

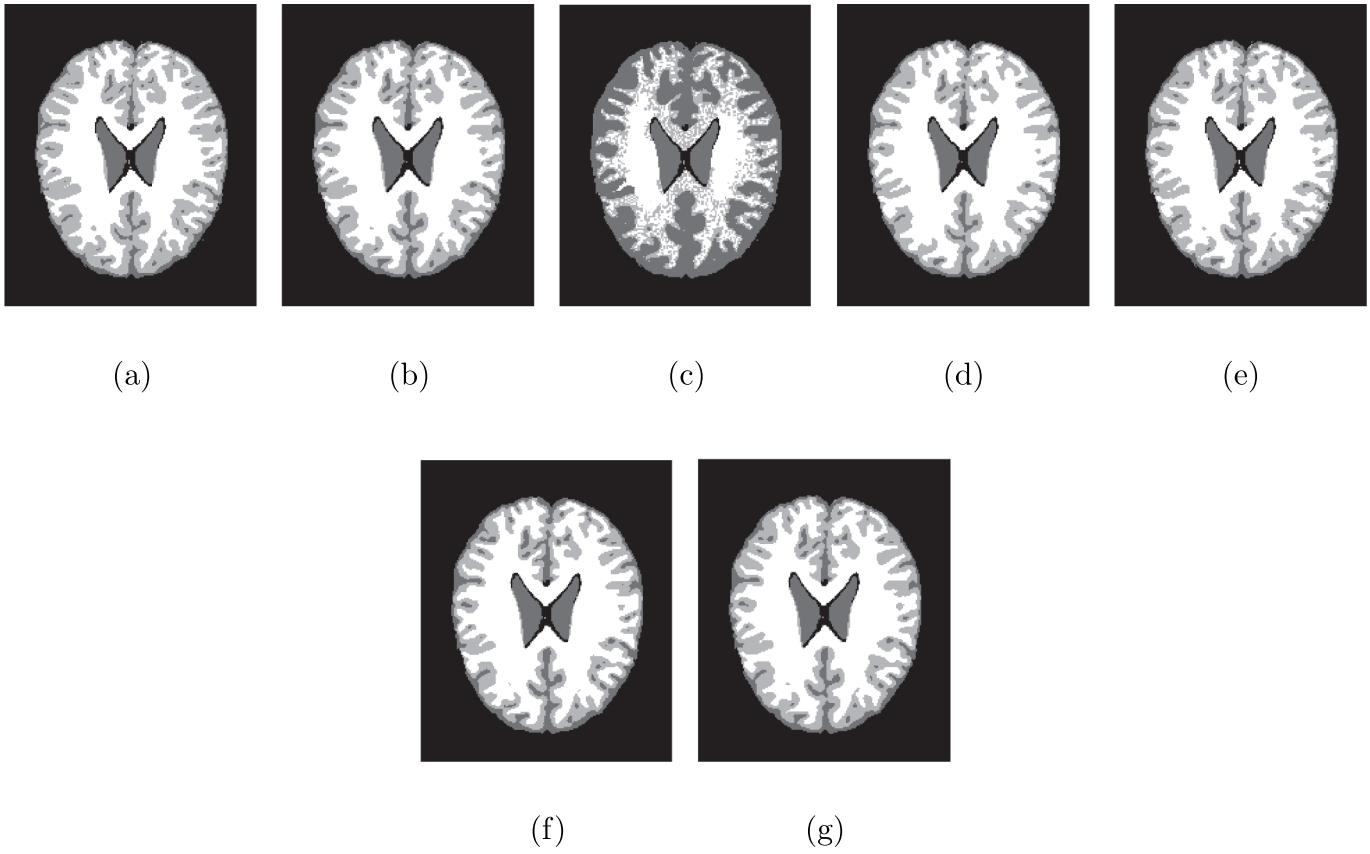

Fig. 5. Brain MRI Z96 plane: (a) Ground truth; and its segmented images obtained by: (b) proposed KRFCMSC, (c) FCM, (d) FCMSC, (e) RFCM, (f) KRFCM, and (g) KSSCM methods.

contingency tables. Then use this global contingency table to compute the micro averaged performance scores. Micro averaged F_1 gives equal weightage on each sample. Micro averaged F_1 is defined as:

$$Micro \quad Averaged \quad F_1 = \frac{2 \times \frac{1}{C}\sum_{i=1}^{C}(p)_i \times \frac{1}{C}\sum_{i=1}^{C} r_i}{\frac{1}{C}\sum_{i=1}^{C} p_i + \frac{1}{C}\sum_{i=1}^{C} r_i}. \tag{22}$$

where, C represents the cluster number. The value of micro averaged F_1 lies between 0 and 1. Closer is the value of micro averaged F_1 to 1 better is the clustering.

- **Kappa:** The Kappa coefficient [55] is a measure of accuracy, it gives a confusion matrix $N_{c\times c}$ of the size $C \times C$ (where, C is the number of cluster), n_{xy} element of the matrix N represents the number of patterns identified into cluster x (x = 1,2,3,.....C) that are similar with cluster y (y = 1,2,3,.....C) in the ground truth dataset. Different indices can be derived from the confusion matrix, sum of all the elements present in the xth row, $n_{x+} = \sum_{y=1}^{C} n_{xy}$ (which is summation of the number of element present in the xth row) and sum of all the element present in the yth column, $n_{+y} = \sum_{x=1}^{C} n_{xy}$. The value of Kappa coefficient lies in the range $[-1, +1]$. Closer is the value of Kappa to + 1, better is the clustering.

Kappa coefficient is defined as:

$$Kappa = \frac{n\sum_{x=1}^{C} n_{xx} - \sum_{x=1}^{C} n_{x+}n_{+x}}{n^2 - \sum_{x=1}^{C} n_{x+}n_{+x}} \tag{23}$$

- **Jaccard coefficient:** Jaccard coefficient [17] also known as intersection over union (IOU), is the ratio of the common pixels present in the input image (L) and the segmented image(M) to the union function or the collection of pixels present in the input image (L) and the segmented output image (M). In other words, Jaccard coefficient is the ratio between the intersection and the union of the pixel values present in the input image (L) and the segmented image (M); and (S) represents the summation function.

$$J(L, M) = \frac{S(L \cap M)}{S(L \cup M)}. \tag{24}$$

Higher is the value of the Jaccard coefficient, better is the segmentation. The range of the Jaccard coefficient lies between 0 and 1. Closer is the value of Jaccard to 1 better is the performance.

- **Dice coefficient (DC):** Dice coefficient [17] value is represented with the help of Jaccard index J(L, M). DC defines the similarity

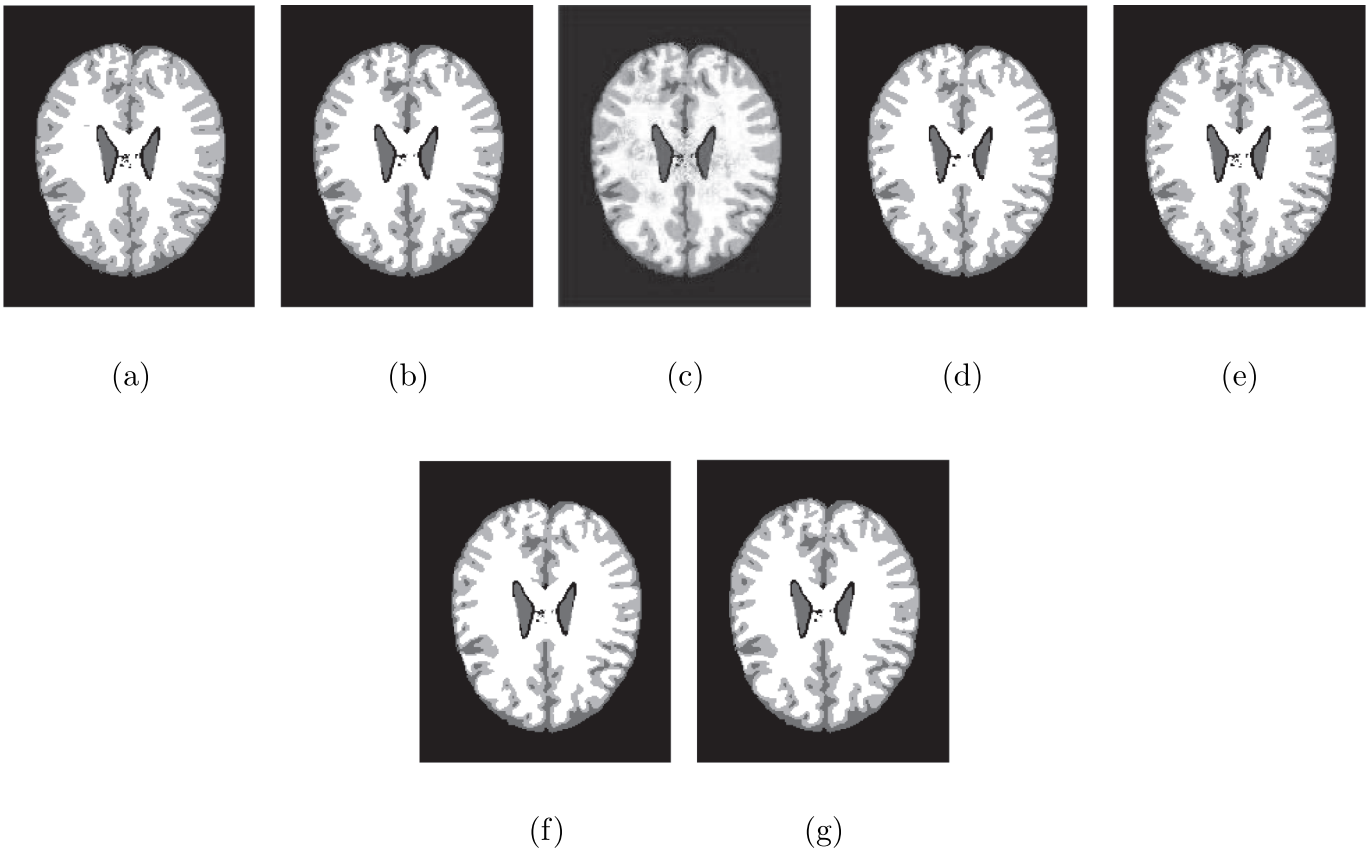

Fig. 6. Brain MRI Z100 plane: (a) Ground truth; and its segmented images obtained by: (b) proposed KRFCMSC, (c) FCM, (d) FCMSC, (e) RFCM, (f) KRFCM, and (g) KSSCM methods.

Table 3
The summary of the average experimental results of 10 simulations in terms of kernelized Xie-Beni index (KXBI) obtained by the proposed KRFCMSC and other compared methods FCM, FCMSC, RFCM, KRFCM, and KSSCM performed on brain MRI data in Z85, Z93, Z96, and Z100 planes.

MRI data	Method	KXBI
Z85	KRFCMSC	2.97E−13
	FCM	1.16E−12
	FCMSC	3.26E−13
	RFCM	4.84E−11
	KRFCM	**3.55E−14**
	KSSCM	6.99E−13
Z93	KRFCMSC	**1.52E−13**
	FCM	1.60E−12
	FCMSC	2.44E−13
	RFCM	4.81E−11
	KRFCM	2.29E−13
	KSSCM	2.96E−13
Z96	KRFCMSC	**1.54E−13**
	FCM	1.60E−12
	FCMSC	1.27E−12
	RFCM	5.00E−11
	KRFCM	1.42E−12
	KSSCM	3.91E−13
Z100	KRFCMSC	9.39E−14
	FCM	2.48E−12
	FCMSC	2.77E−13
	RFCM	5.50E−11
	KRFCM	1.96E−12
	KSSCM	**7.96E−14**

Table 4
The summary of the average experimental results of 10 simulations in terms of kernelized Xie-Beni index (KXBI) obtained by the proposed KRFCMSC and other compared methods FCM, FCMSC, RFCM, KRFCM, and KSSCM performed on brain MRI data IBSR144, IBSR150, IBSR155, and IBSR167.

MRI data	Method	KXBI
IBSR144	KRFCMSC	**6.73E−15**
	FCM	7.26E−14
	FCMSC	2.05E−14
	RFCM	4.89E−11
	KRFCM	1.65E−12
	KSSCM	1.37E−14
IBSR150	KRFCMSC	**3.15E−15**
	FCM	6.88E−13
	FCMSC	1.01E−13
	RFCM	8.71E−11
	KRFCM	1.82E−13
	KSSCM	6.39E−15
IBSR155	KRFCMSC	7.84E−15
	FCM	4.97E−13
	FCMSC	1.27E−13
	RFCM	5.02E−11
	KRFCM	3.13E−14
	KSSCM	**4.42E−15**
IBSR167	KRFCMSC	**3.75E−16**
	FCM	2.74E−13
	FCMSC	7.52E−14
	RFCM	4.69E−11
	KRFCM	3.57E−13
	KSSCM	1.82E−15

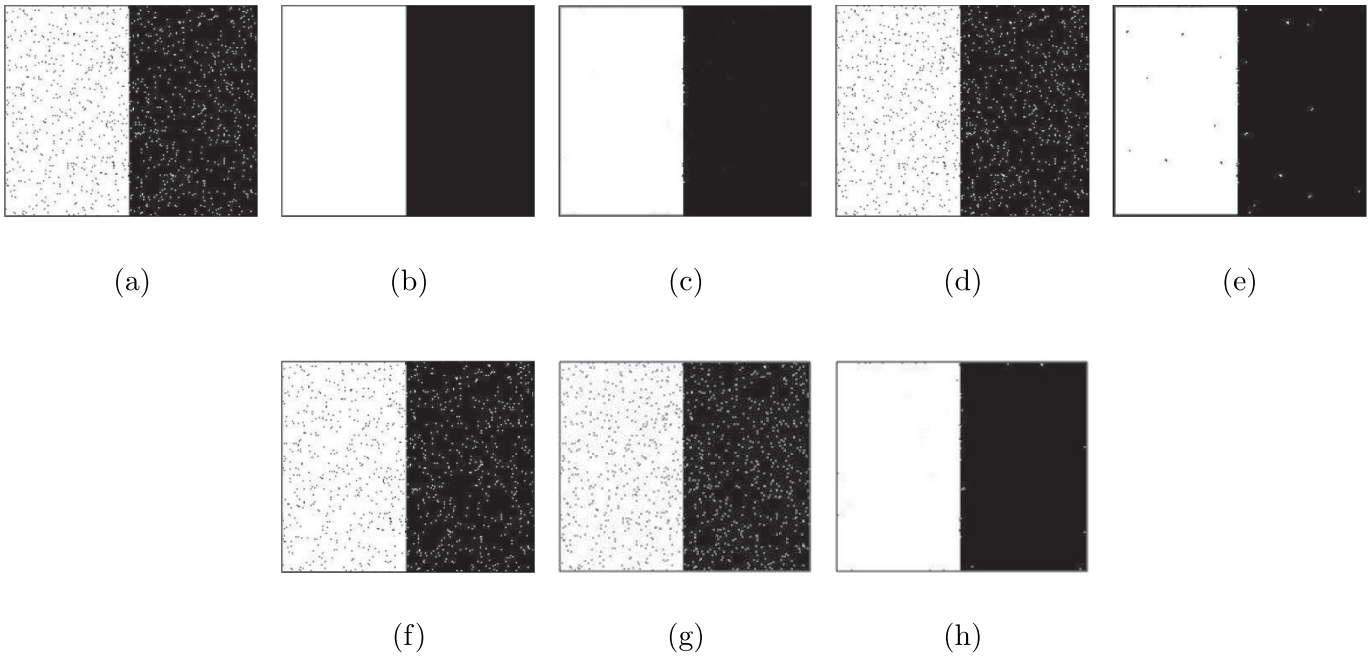

Fig. 7. (a) Synthetic image with 6% "salt and pepper" noise, (b) its corresponding ground truth; also the segmented images obtained by: (c) proposed KRFCMSC, (d) FCM, (e) FCMSC, (f) RFCM, (g) KRFCM and (h) KSSCM.

Table 5
Result of paired *t*-tests performed on the segmented accuracy obtained by the proposed KRFCMSC versus other compared methods in terms of *p*-score for BrainWeb brain MRI datasets.

MRI data	KRFCMSC vs. KRFCM	KRFCMSC vs. RFCM	KRFCMSC vs. FCMSC	KRFCMSC vs. FCM	KRFCMSC vs. KSSCM
Z85	**4.6710E−07**	**2.3492E−07**	**3.1498E−05**	**1.4081E−07**	**0.0309**
Z93	**9.3811E−04**	**6.3500E−06**	**2.1014E−04**	**1.3375E−04**	0.3363
Z96	**3.7969E−08**	**6.5396E−07**	**8.1524E−07**	**3.5043E−07**	**0.0458**
Z100	**2.4064E−06**	**8.4346E−07**	**8.6037E−06**	**2.3159E−07**	0.3527

Table 6
Result of paired *t*-test performed on the segmented accuracy obtained by the proposed KRFCMSC versus other compared methods in terms of *p*-score for IBSR brain MRI datasets.

MRI data	KRFCMSC vs. KRFCM	KRFCMSC vs. RFCM	KRFCMSC vs. FCMSC	KRFCMSC vs. FCM	KRFCMSC vs. KSSCM
IBSR144	**0.0015**	0.1721	**0.0286**	**0.0023**	0.1009
IBSR150	**0.0162**	0.1780	0.1293	**0.0070**	**0.0452**
IBSR155	0.3908	0.5759	0.7550	**0.0317**	0.6689
IBSR167	**0.0068**	**0.0229**	0.0508	**2.4197E−05**	**0.0171**

Table 7
The summery of the average segmentation accuracies in % of 10 simulations obtained by different methods performed on synthetic image of (Fig. 7) corrupted with 6% "Salt and Pepper" noise.

Noise type	KRFCMSC	FCM	FCMSC	RFCM	KRFCM	KSSCM
Salt & pepper	**98.99**	91.56	96.39	92.41	94.14	98.41

Table 8
The summery of the average segmentation accuracies in percentage of 10 simulations obtained by different methods performed on BrainWeb brain MRI datasets corrupted with 6% "Salt and pepper" noise.

MRI data	KRFCMSC	FCM	FCMSC	RFCM	KRFCM	KSSCM
Z85	**93.61**	84.91	88.80	83.21	84.11	92.86
Z93	**94.29**	85.63	90.17	89.02	89.37	93.77
Z96	91.10	89.01	89.13	89.00	89.06	**91.36**
Z100	**93.89**	85.79	88.07	87.46	87.71	93.07

function of the input image (L) and the segmented output image (M) and can be defined as:

$$D(L, M) = 2 \times \frac{J(L, M)}{1 + J(L, M)}. \quad (25)$$

The range of the Dice coefficient lies between 0 and 1. Closer the value of Dice to 1 better is the segmentation.

- **Kernelized Xie-Beni index (KXBI):** It is a unsupervised cluster validity measure. It defines the inter-cluster separation as the

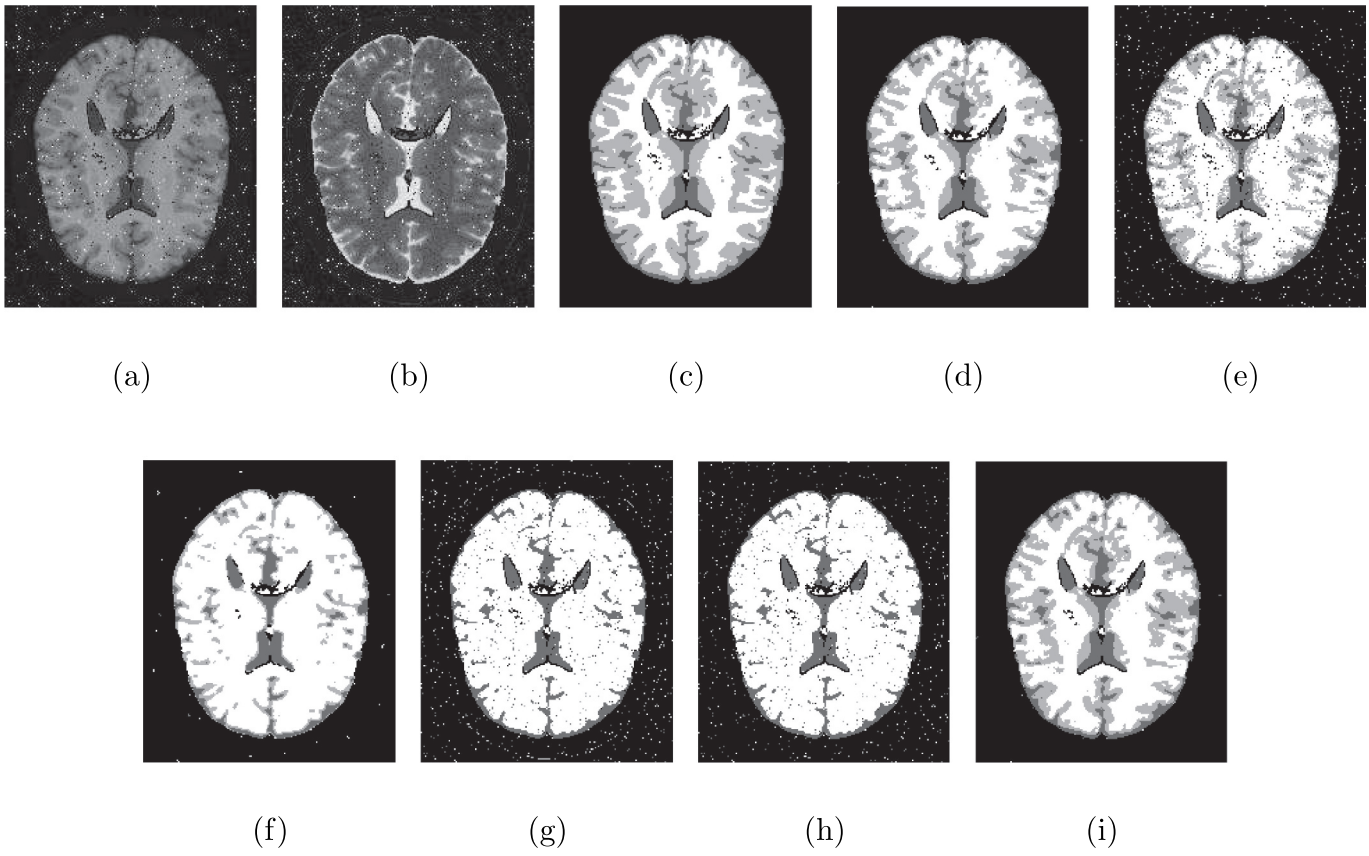

Fig. 8. (a) T1-weighted, (b) T2-weighted brain MRI in Z85 plane corrupted with 6% "salt and pepper" noise; (c) its corresponding ground truth; also the segmented images obtained by: (d) proposed RFCMSC, (e) FCM, (f) FCMSC, (g) RFCM, (h) KRFCM, and (i) KSSCM.

Table 9
The summery of the average segmentation accuracies in percentage of 10 simulations obtained by different methods performed on BrainWeb and IBSR brain MRI datasets corrupted with 5% "rician" noise.

MRI data	KRFCMSC	FCM	FCMSC	RFCM	KRFCM	KSSCM
Z85	**93.73**	85.17	89.30	85.09	85.31	93.20
Z100	**93.81**	85.99	88.57	86.86	88.1	93.19
IBSR 144	90.01	84.11	88.17	88.02	87.19	**90.24**
IBSR 150	**91.13**	89.21	90.10	90.09	88.25	90.68

minimum square distance between the centers of the clusters, and the intra-cluster compactness as the mean square distance between each pixel and its cluster center. Lower the value of KXBI better is the cluster quality [56]. The range of the KXBI lies between 0 and 1. Kernelized Xie-Beni index is defined as:

$$KXBI = \frac{2 \times \sum_{k=1}^{n} \left\{ \sum_{j=1}^{c} (1 - \mathbb{K}(\vec{x_k}, \vec{v_j})^{\frac{1}{1-m}})^{(1-m)} \right\}}{n \times min_{i \neq j} [2 \times \{1 - \mathbb{K}(\vec{v_i}, \vec{v_j})\}]}. \quad (26)$$

Lower is the value of the kernelized Xie-Beni index, better is the segmentation. The range of the kernelized Xie-Beni index lies between 0 and 1.

5. Results and discussion

Experiments have been performed on as many as 30 brain MRI from IBSR datasets as well as from BrainWeb datasets of different Z planes with and without added noise; out of which only few representative experimental results in terms of various supervised and unsupervised validity measures along with the corresponding segmented brain MRI output images obtained by the different methods are reported for the BrainWeb data Z85 (Fig. 3), Z93 (Fig. 4), Z96 (Fig. 5), and Z100 (Fig. 6)) and as well as for IBSR data IBSR144, IBSR150, IBSR155 (shown in Fig. 11 in Tables 1 and 2 respectively). The ground truth images for the IBSR dataset provided in the database [48] are shown in the second row (e)–(h) in Fig. 11 for IBSR144, IBSR150, IBSR155, and IBSR167 respectively, and the ground truth images for BrainWeb dataset (provided in the database [47]) are shown in the first row

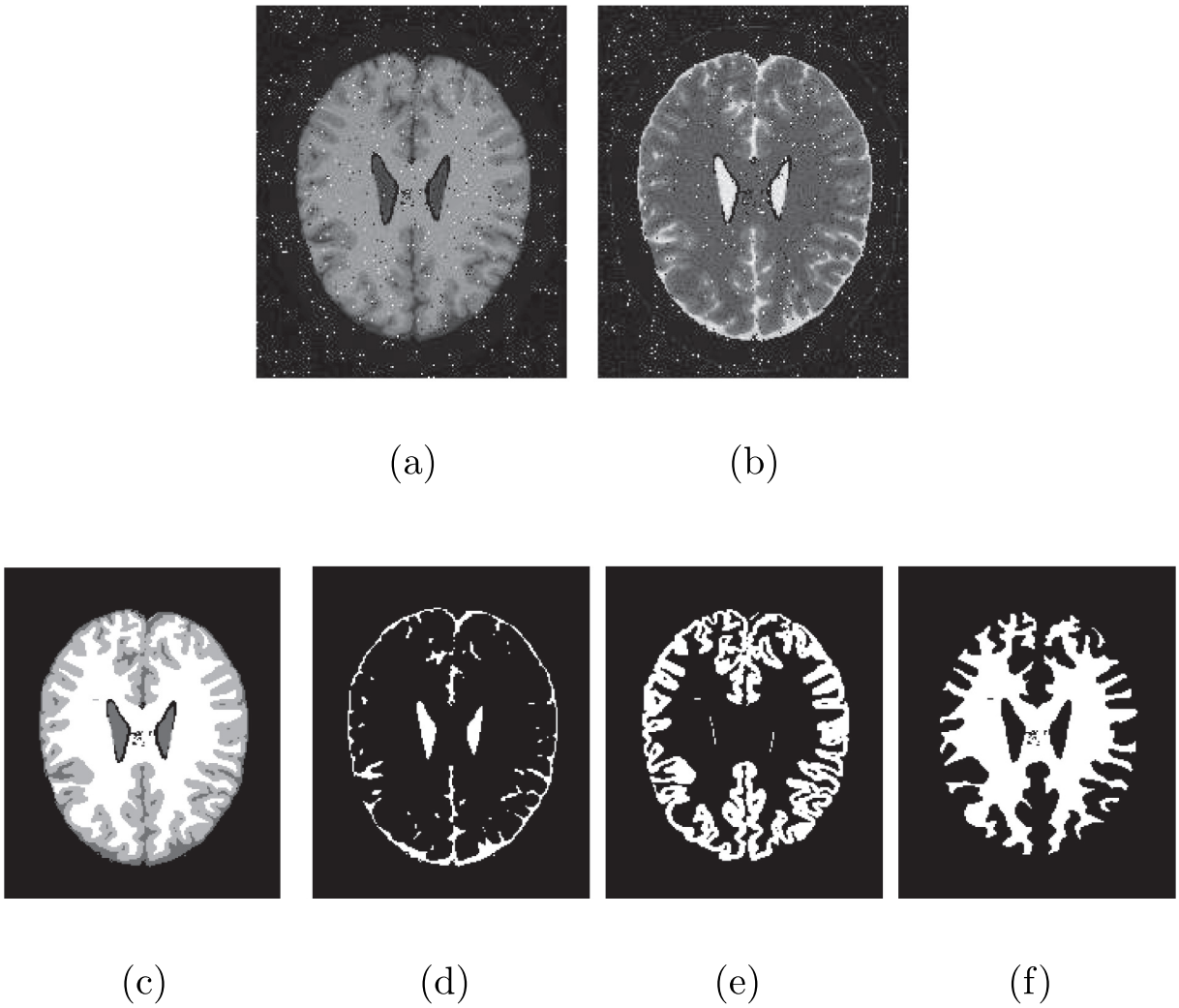

Fig. 9. Brain MRI Z100 plane: First row: (a) T1-weighted and (b) T2-weighted: images added with 6% "salt and pepper" noise. Second row: (c) overall ground truth, (d) CSF, (e) GM and (f) WM represents overall and individual ground truths of different segments.

((a)–(d)) of Fig. 3 for brain MRI Z85, and subfigure (a) in Figs. 4–6 for Z93, Z96, and Z100 (with every corresponding brain MRI planes Z85, Z93, Z96, and Z100 in Fig. 1). Note that; the ground truths for BrainWeb dataset are constructed from the information supplied in the database [47] taking the major brain segments (i.e., CSF, GM, WM) and assign the pixel in the corresponding segment for which fuzzy membership (given in the database as fuzzy ground truth) is the highest. The other non (major) brain segments are considered as background shown as black color in the ground truth images.

The best results in terms of the above said validation indices for each data are made bold for the corresponding method in Tables 1–4.

Segmented images obtained by the proposed KRFCMSC method and the different counterpart clustering based techniques are summarized in Fig. 3 for BrainWeb brain MRI Z85 plane (ground triuth of which is shown in Fig. 2).

Likewise, Figs. 4–6 summarize the ground truths and the segmented images obtained by the proposed algorithm and the comparing methods for BrainWeb MRI in Z93, Z96, and Z100 planes respectively. The results of the validity indices considered are shown in Tables 1–4. From the summarized results, it is seen that the proposed method KRFCMSC outperformed the other compared methods in terms of segmented accuracy. The improvements in segmentation accuracy achieved by proposed method for Z85 are 8.33%, 3.27%, 3.98%, 2.87%, and 0.62% respectively with FCM, FCMSC, RFCM, KRFCM, and KSSCM methods.

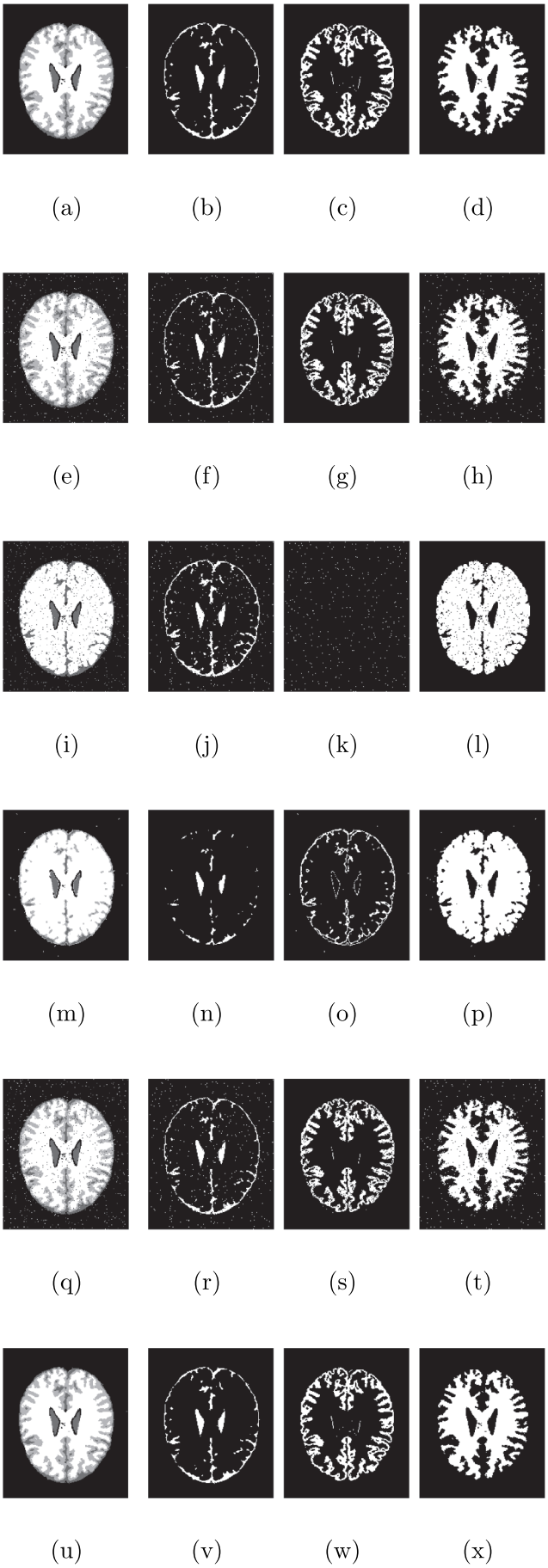

Fig. 10. Brain MRI Z100 plane: segmented images (of Fig. 9). First row ((a) overall segmented image, individual segmented images of different segments viz., (b) CSF, (c) GM and (d) WM) obtain by the proposed KRFCMSC. Second row by KRFCM. Third row by FCM. Fourth row by FCMSC. Fifth row by RFCM. Sixth row by KSSCM.

Similarly, for Z93 image the performances of the proposed method are improved by 6.4%, 3.53%, 4.37%, 2.71%, and 0.52% with respect to FCM, FCMSC, RFCM, KRFCM, and KSSCM. Likewise, for Z96 the improvements in accuracies obtained by the proposed method compared to its nearest competitive algorithms is 0.55% (see Table 1).

From Fig. 3 to Fig. 6, it can be observed that the proposed KRFCMSC method detects all the different segments almost accurately, whereas, the other compared algorithms fail to detect some portions of the different segments properly.

In Fig. 11, IBSR datasets are summarized with their corresponding ground truths. Whereas, in Fig. 12 segmented results of the proposed method KRFCMSC and the different counterpart clustering based techniques are summarized for IBSR brain MRI IBSR144, IBSR150, IBSR155, and IBSR167. The dominance of the proposed method KRFCMSC over other compared methods can be verified from the segmented images (in Fig. 12) as well as from the different validity indices values (in Table 2 and in Table 4).

From the visual observation as well as from the validity indices value (recoded in Tables 1 and 2), it is seen that the proposed KRFCMSC outperforms the compared methods for all the datasets except brain MRI IBSR155.

To test the robustness, the proposed KRFCMSC method is also simulated with binary synthetic image corrupted with 6% “salt & pepper” noise as shown in Fig. 7. Where, Fig. 7 (b) is the ground truth of Fig. 7 (a). Fig. 7 (c)–(h) are the corresponding segmented images produced by the proposed method KRFCMSC, and different compared algorithms. From the segmentation accuracy summarized in Table 7 and as well as from the segmented images (visual observations), it can be noticed that the proposed technique outperformed the other compared algorithms as the noise present in the segmented image produced by the proposed algorithm is least.

The proposed technique is also tested with 6% added “salt and pepper” noise and 5% added “rician” noise in brain MRI (same set of brain MRI used earlier). From the summarized experimental results in Table 8, it is seen that for brain MRI Z85 the proposed method KRFCMSC dominates all the other compared methods in terms of segmented accuracy. Here, the improvements in segmented accuracy obtained by proposed method are 8.7%, 4.81%, 10.4%, 9.5%, and 0.75% (see Table 8) with respect to FCM, FCMSC, RFCM, KRFCM, and KSSCM respectively. From the visual observation also in Fig. 8 it can be seen that except the proposed method all the other methods missed to detect the gray matter (GM) accurately. Likewise in brain MRI Z100 also, proposed method outperformed the other methods by 8.1%, 5.82%, 6.43%, 6.18%, and 0.82% (see Table 8) improvements in segmentation accuracy as compared respectively to FCM, FCMSC, RFCM, KRFCM, and KSSCM. Similar observations are also found for brain MRI Z planes Z93 and Z96. For the images corrupted with “rician” noise also revel similar observations (see Table 9) as with “salt and pepper” noise which are summarized in Fig. 13 and in Fig. 14.

Finally, in Fig. 10 ground truths as well as segmented outputs of the proposed method KRFCMSC and the different counterpart clustering based techniques are summarized for brain MRI Z100 plane corrupted with 6% “salt and pepper” noise. Here typical representative result (as done in Fig. 3) of individual segmented images for different regions are also shown in different figures.

From Fig. 10 it can be seen that only the proposed KRFCMSC method detects all the different segments accurately, with least or almost no noise present. Whereas, the other compared methods (in particular, FCM, RFCM, and KRFCM) fail to detect particularly the gray

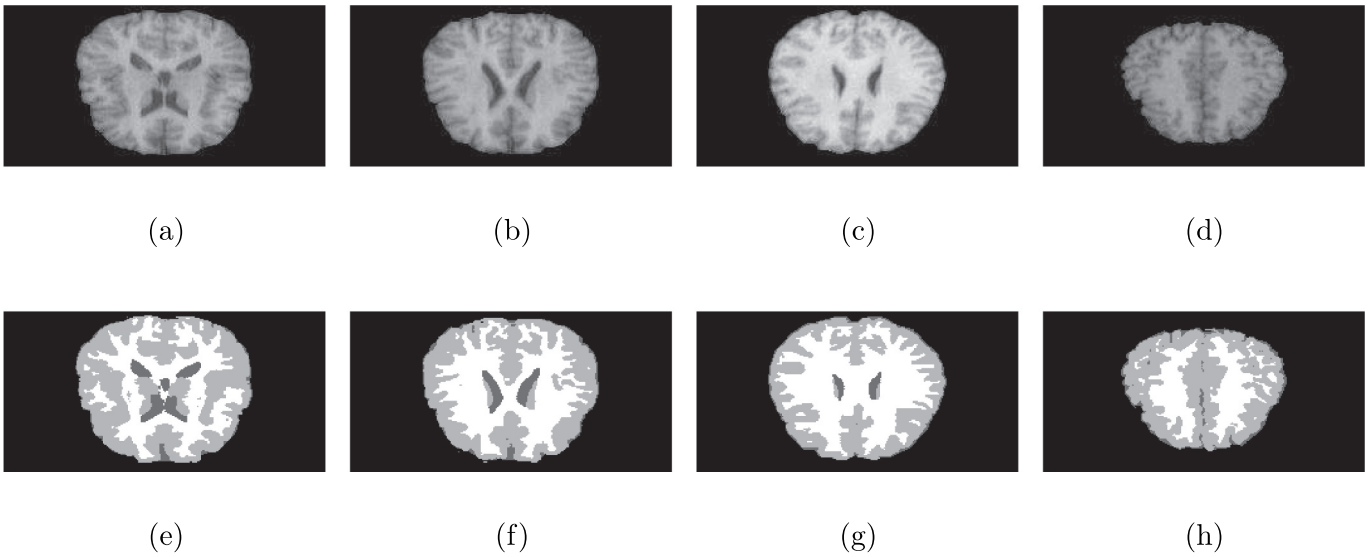

Fig. 11. First row represents the IBSR brain MRI data (a) IBSR144, (b) IBSR150, (c) IBSR155, and (d) IBSR167. Second row (e)–(h) represents their corresponding ground truths.

matter accurately.

Experimental results turned out to be similar for other brain MRI scans. In summary, the proposed KRFCMSC method clearly generates better segmentation result for all the brain MRI dataset compared to that of its other counterpart clustering based segmentation algorithms both in terms of the visualization quality of the segmented images as well as from the validity indices. The proposed method also performs better compared to other counterpart methods in segmenting the images corrupted with “salt and pepper” and “rician” noises.

Further, execution time of the proposed method as well as the other counterpart methods are summarized in Table 10. From the experimental observations its seen that the proposed method takes little more execution time (except KSSCM method in some cases) than those taken by the other compared methods. Execution time of the proposed method is little higher because of the use of kernel function and the concept of spatial constraints from the neighbouring pixels in the clustering process. However, at the cost of little more execution time (around 10 to 20 s) the proposed method achieved significantly better accuracy compared to other methods for brain tissue segmentation from MRI.

Performance of the proposed technique is influenced by the parameters namely, fuzziness index m, w_{low} (or $w_{up} = 1 - w_{low}$), controlling parameter α (that controls the effect of the neighbouring term) and *threshold*. The parameter values viz., m, w_{low}, α, and *threshold* are empirically determined for optimum performance of the algorithm as 2, 0.8, 1, and 0.8 respectively. However, the value of the threshold and other parameters can also be estimated by optimizing techniques like Genetic Algorithms (GA) and Particle Swarm Optimization (PSO) etc in future and needless to mention that it will increase the time complexity of the overall clustering.

5.1. Box-plot

The Box-and-Whisker plots [57] (popularly known as Box-plot, in this article we will call Box-and-Whisker plots as Box-plot for the simplicity) of percentage accuracy achieved by different segmentation algorithms performed 10 simulations on BrainWeb, and IBSR brain MRI datasets are shown respectively in Figs. 15 and 16. From Fig. 15 it can be noticed that, for most of the BrainWeb datasets (viz., Z85, Z93, Z96, and Z100) the Box-plots are relatively more dense for the proposed technique as compared to those obtained with other compared algorithms, which points to the fact that the results (in terms of percentage segmentation accuracy (SA)) achieved by the proposed algorithm for 10 simulation runs have quite similar performance in terms of segmentation accuracy with less standard deviations (SD) than those achieved by the other compared algorithms. Also, the median values of the segmentation accuracies achieved by the proposed method are quite higher than those achieved with other methods for the above said datasets as shown in Fig. 15. Box-plot results turned out to be similar for the IBSR dataset except IBSR155 as shown in Fig. 16. From the fact it can be concluded that the segmentation accuracy in terms of accuracies achieved by the proposed method outperformed the other compared clustering based segmentation algorithms.

5.2. Significance test

Significance of the experimental results (of 10 simulation runs in terms of percentage segmented accuracy) are confirmed statistically

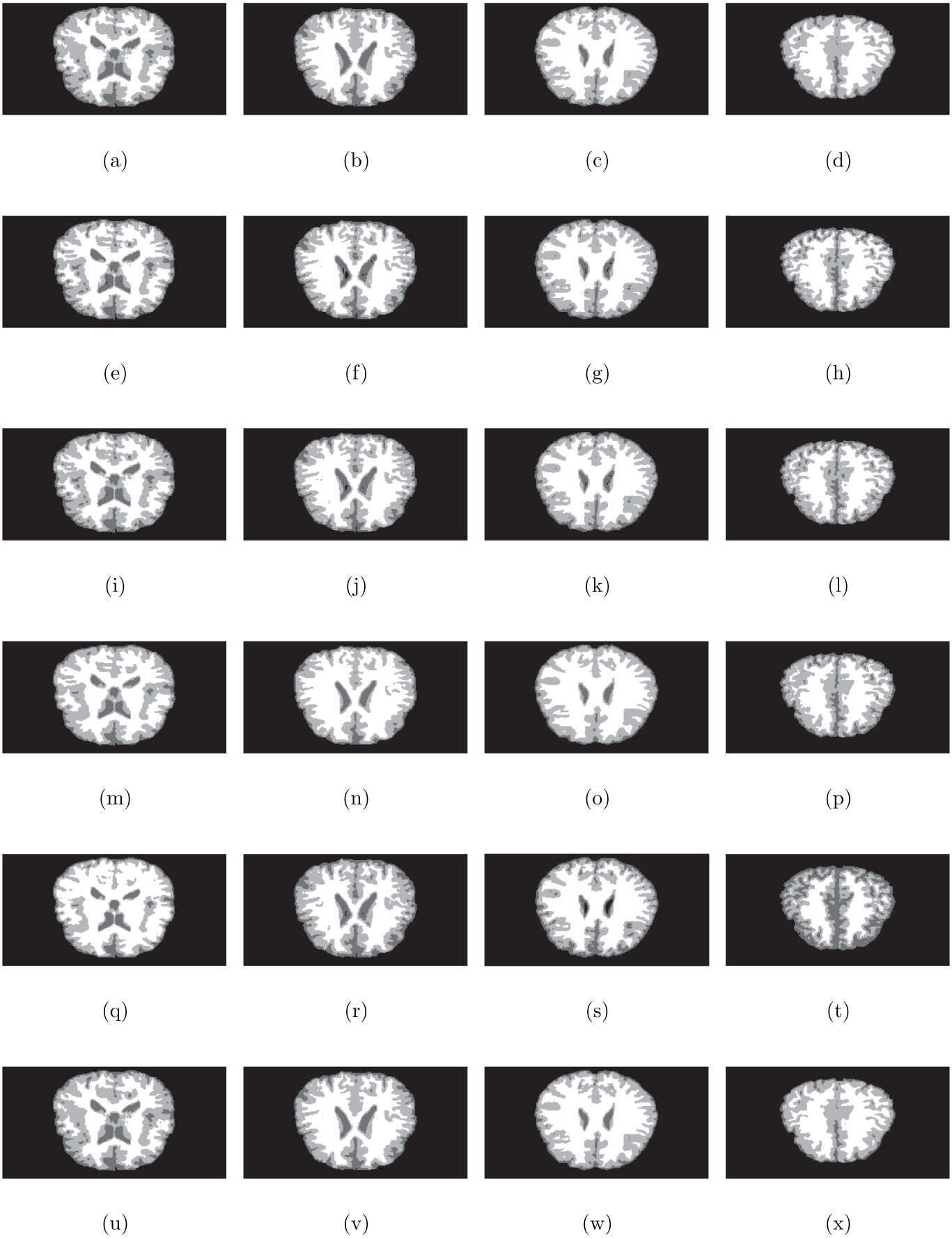

Fig. 12. Segmented results of Fig. 11 by different methods: First row (a)–(d) obtain by the proposed KRFCMSC. Second row (e)–(h) by KRFCM. Third row (i)–(l) by RFCM. Fourth row (m)–(p) by FCMSC. Fifth row (q)–(t) by FCM. Sixth row (u)–(x) by KSSCM.

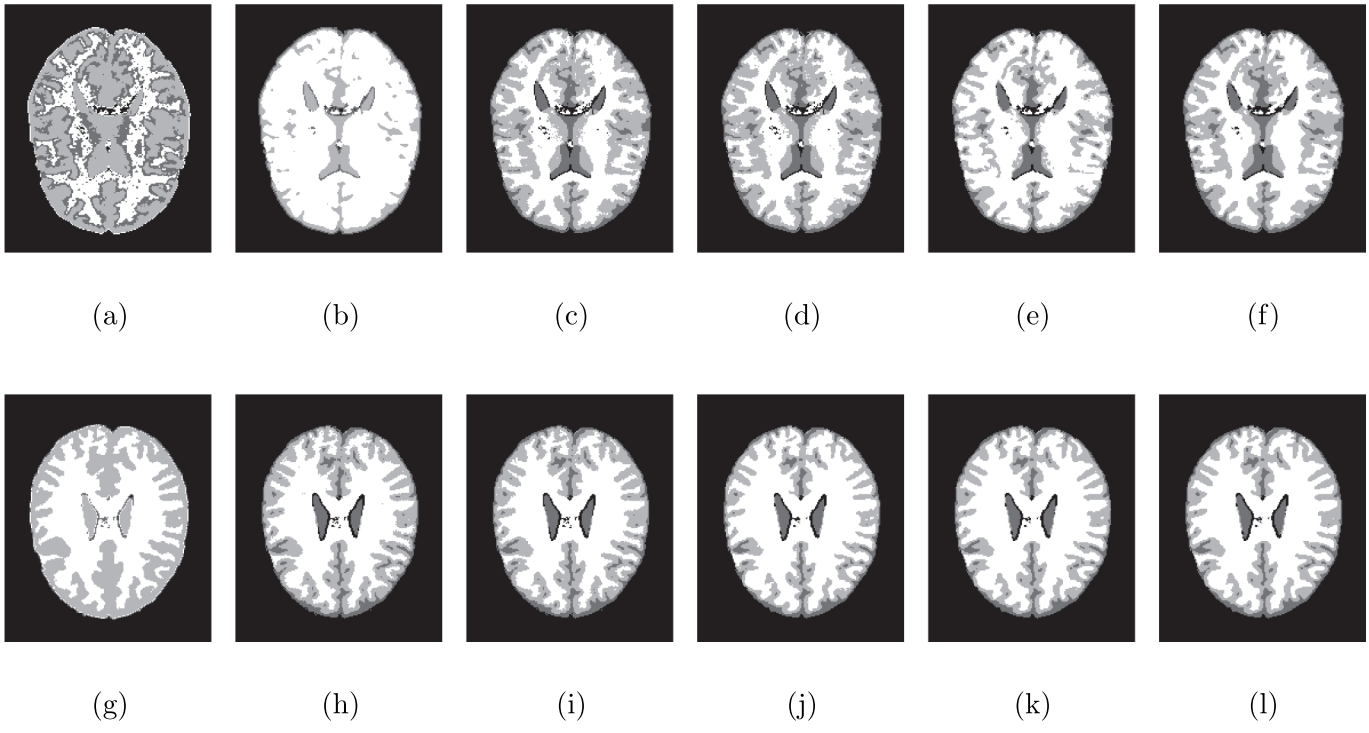

Fig. 13. Segmented results of BrainWeb data sets Z85 and Z100 (used earlier) corrupted with 5% rician noise: First row, segmented results by (a) FCM, (b) RFCM, (c) KRFCM, (d) FCMSC, (e) KSSCM and (f) proposed KRFCMSC performed on Z85. Second row, segmented results by (g) FCM, (h) RFCM, (i) KRFCM, (j) FCMSC, (k) KSSCM and (l) proposed KRFCMSC performed on Z100.

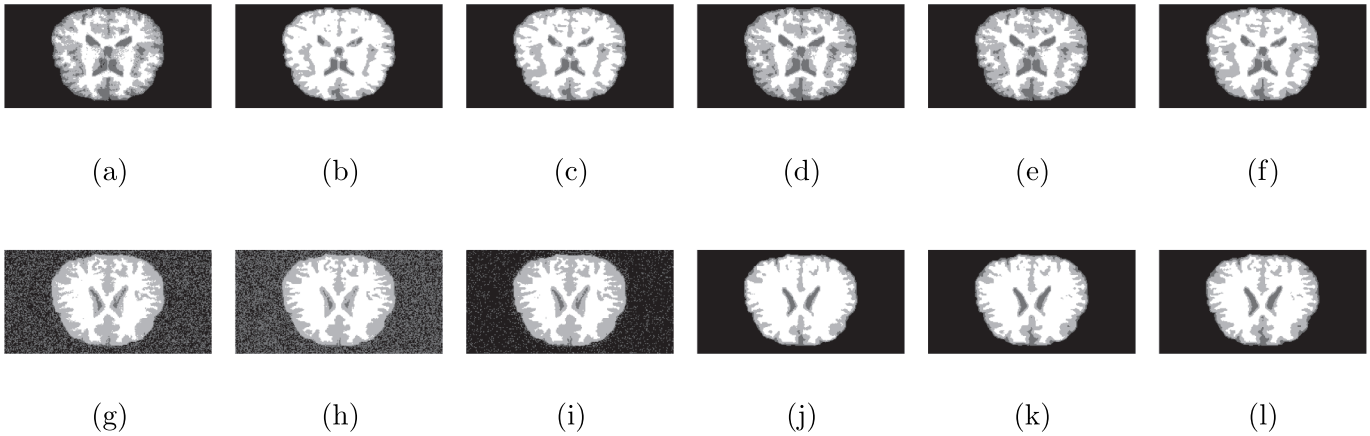

Fig. 14. Segmented results of IBSR 144 and IBSR 150 (used earlier) corrupted with 5% rician noise: First row, segmented results by (a) FCM, (b) RFCM, (c) KRFCM, (d) FCMSC, (e) KSSCM and (f) proposed KRFCMSC performed on IBSR 144. Second row, segmented results by (g) FCM, (h) RFCM, (i) KRFCM, (j) FCMSC, (k) KSSCM and (l) proposed KRFCMSC performed on IBSR 150.

using the paired *t*-test [58] results obtained by the proposed KRFCMSC versus other compared clustering based segmentation algorithms at 5% level of significance for IBSR (MRI IBSR144, IBSR150, IBSR155 and IBSR167) as well as for BrainWeb (MRI Z85, Z93, Z96, and Z100) datasets. The null hypothesis of the test presumes that there is no significant difference between the two sets of results achieved by the proposed algorithm and different compared algorithms. *t*-test results achieved by the proposed KRFCMSC method versus other clustering methods in terms of *p*-score are recoded in Table 5 and in Table 6 for BrainWeb and IBSR dataset respectively. Results of *t*-test are statistically significant (at 5% level of significance) if the corresponding *p* value is less than or equal to 0.05, suggesting that the null hypothesis is rejected i.e., there exists statistically significant difference in the results (in terms of percentage segmented accuracy) achieved by the compared and comparing methods. Results of the *t*-test suggest that the segmented accuracy (SA) achieved by the proposed KRFCMSC algorithm

Table 10
Summary of the execution time in second (of 10 simulations) obtained by the proposed method KRFCMSC and other compared methods FCM, FCMSC, RFCM, KRFCM, and KSSCM performed on various IBSR and BrainWeb brain MRI datasets.

MRI data	Method					
	FCM	FCMSC	RFCM	KRFCM	KSSCM	KRFCMSC
IBSR144	74.02	76.12	79.24	80.16	86.14	84.08
IBSR150	71.08	72.03	76.18	79.11	84.08	84.10
IBSR155	69.55	71.20	74.18	77.30	82.32	83.24
IBSR167	73.16	74.22	77.08	83.14	88.24	87.20
Z85	70.12	72.20	76.24	80.50	87.10	87.09
Z93	69.20	73.24	78.22	81.08	89.16	90.04
Z96	67.26	70.18	72.48	79.08	85.08	82.42
Z100	69.10	71.22	74.34	79.02	88.20	90.08

significantly dominates other counterpart algorithms except for 2 cases marked in normal font in Table 5 for BrainWeb datasets. In case of IBSR datasets out of total 20 paired *t*-tests performed, the proposed method significantly dominates other methods in 11 cases as shown in bold font in Table 6.

In summary, out of 40 (20 for BrainWeb and 20 for IBSR datasets) paired *t*-tests performed by the proposed KRFCMSC versus other counterpart methods, in 29 cases the proposed method achieved statistically significant improvements in segmentation accuracy compared to other algorithms. Therefore, the efficiency of the proposed KRFCMSC algorithm (for MRI brain segmentation) compared to other clustering based segmentation algorithm is well evident from the paired *t*-test results for brain MRI segmentations (viz., IBSR dataset and BrainWeb dataset) for most of the datasets.

Study turned out to be similar for other brain MRI dataset with and without noise. In summary, the proposed method KRFCMSC generates

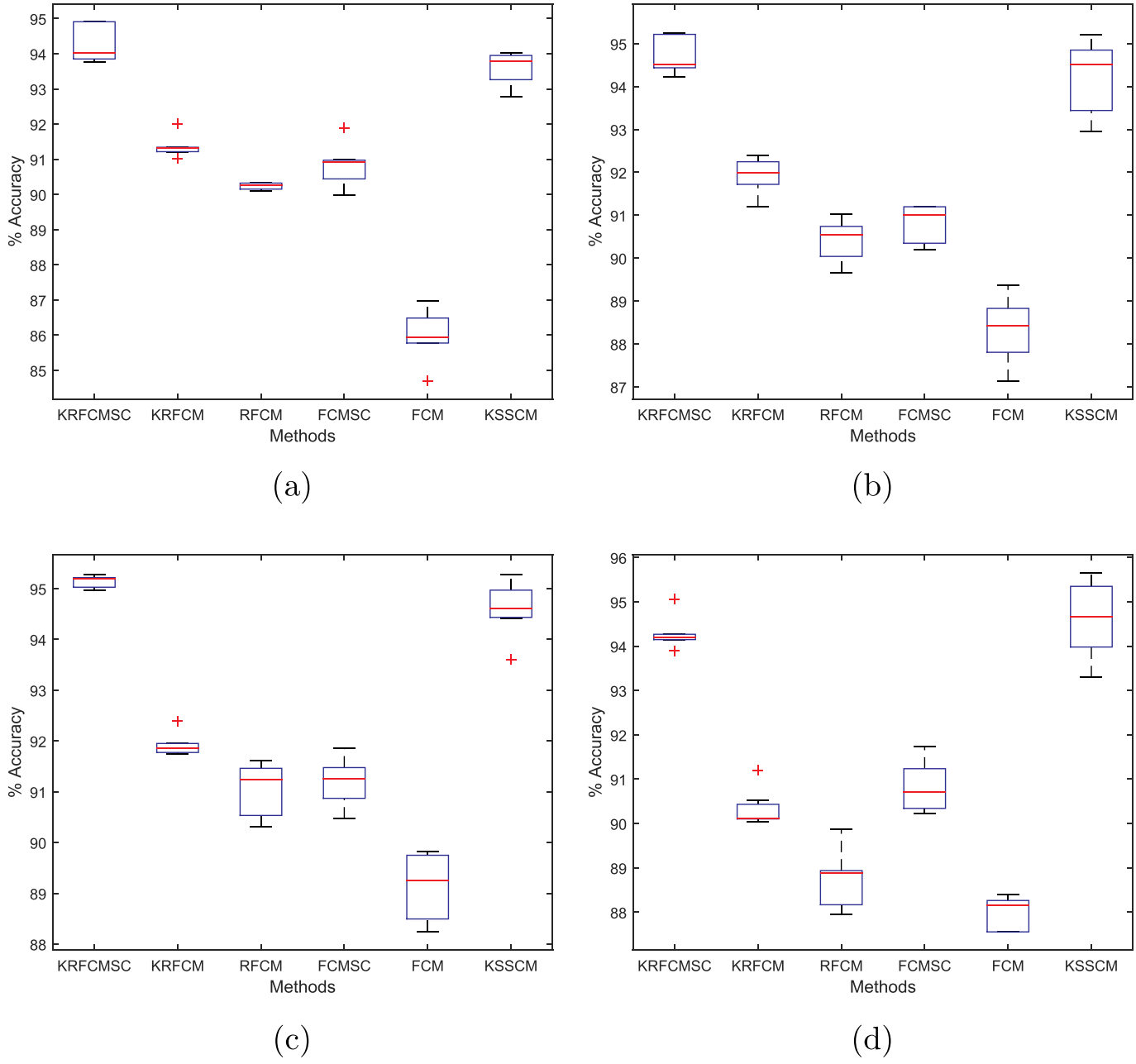

Fig. 15. Boxplots of accuracies obtained using proposed method KRFCMSC and other counterpart methods viz., FCM, FCMSC, RFCM, KRFCM and KSSCM different clustering algorithms performed on brain MRI datasets in different Z planes: (a) Z85, (b) Z93, (c) Z96, and (d) Z100.

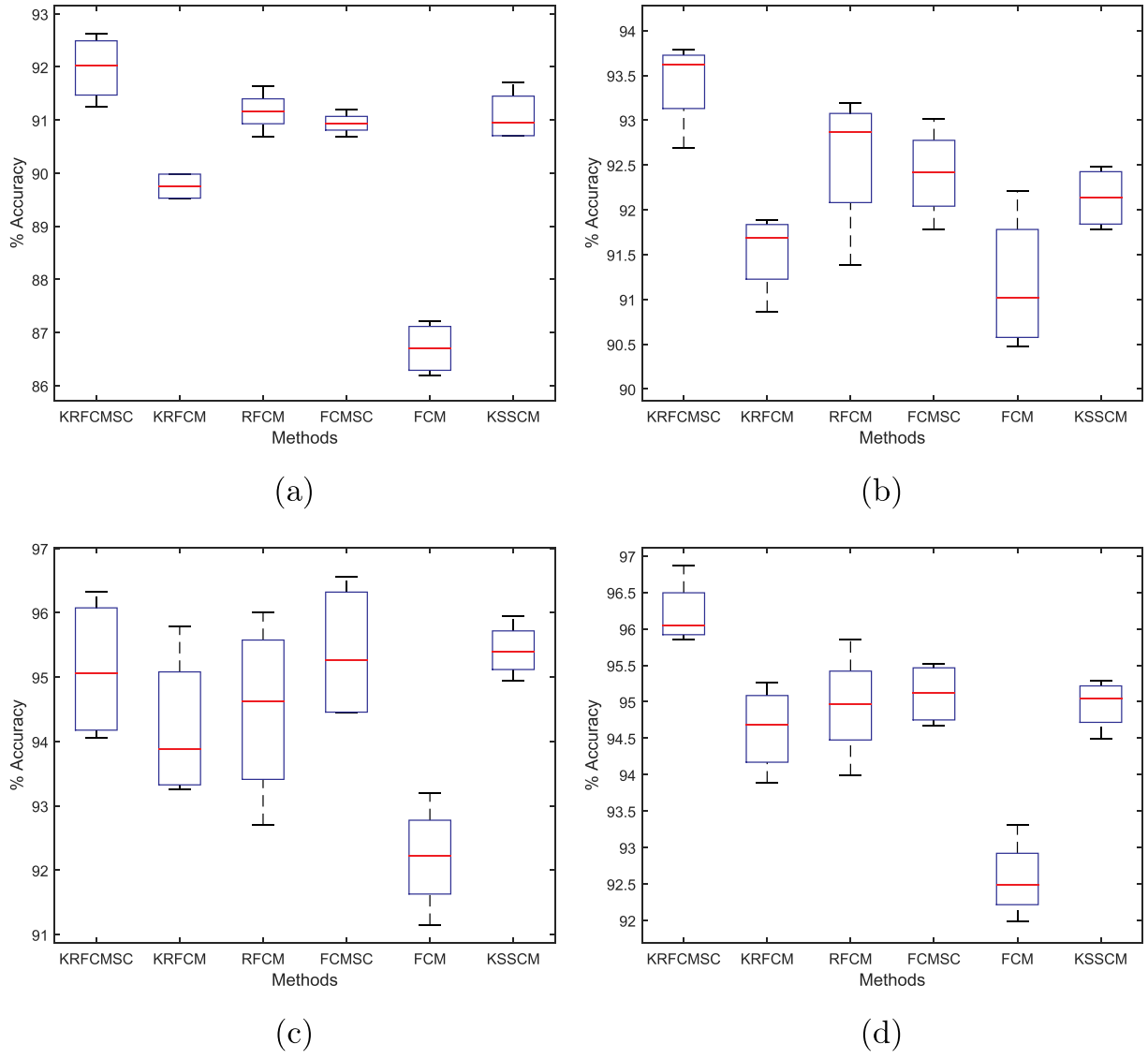

Fig. 16. Boxplots of accuracies obtained using proposed method KRFCMSC and other counterpart methods viz., FCM, FCMSC, RFCM, KRFCM and KSSCM different clustering algorithms performed on brain MRI datasets: (a) IBSR144, (b) IBSR150, (c) IBSR155, and (d) IBSR167.

better segmentation in brain MRI compared to other counterpart clustering based segmentation algorithms both in terms of considered validation indices as well as from the segmented results.

6. Conclusion

Brain tissue segmentation from MRI is an important task for early detection of any abnormalities. However, the brain MRI tissue segmentation becomes difficult as they generally are indiscernible, ambiguous, and overlapping in nature. Also different tissue regions are not linearly separable. Moreover noises and other artifacts may affect the brain MRI which lower down the segmentation accuracy. To address these issues, in this article, a robust *kernelized rough fuzzy C-means clustering with spatial constraints* (KRFCMSC) is proposed for brain tissue segmentation from MRI.

The idea to use the rough and fuzzy set in the clustering process is to deal the ambiguity, indiscernibility, vagueness and overlappingness of different brain tissue regions commonly present in the brain MRI. Use of the kernel trick here address the non-linear separability issues of the brain tissue regions by projecting the pixels into higher dimension

which increases the chance of linear separability in the projected (higher) dimensional space. While the spatial constraints are used in the clustering process to incorporate the contextual information in order to deal the noisy and outlier effects.

Experiments have been performed on various real and synthetic benchmark brain MRI datasets from BrainWeb (available at http://brainweb.bic.mni.mcgill.ca/brainweb/) and IBSR (https://www.nitrc.org/projects/ibsr/) without and with added noise.

Segmentation results are quantitatively evaluated using various supervised and unsupervised performance validation measures (viz., segmentation accuracy (SA), recall, precision, micro averaged F_1 measure, macro averaged F_1 measure, Jaccard, dice, Kappa, and kernelized Xie-Beni index (KXBI)).

Comparative analysis of the brain tissue segmentation of the proposed method is carried out with respect to five various counterpart algorithms namely, FCM, RFCM, FCMSC, KRFCM, and KSSCM. Robustness and superiority of the proposed algorithm can be validated from the results of experiments for MRI brain tissue segmentation compared to other algorithms. Statistical significance of the better results obtained by proposed technique (in comparison to other methods) can be confirmed from the *t*-test results and Box-plots. Effort may also be made to automatically optimize the parameter values in future.

Declaration of Competing Interest

We hereby declare that there is no conflict of interest in this research work.

Acknowledgments

We are thankful to the anonymous reviewers and editor for their comments to improve the manuscript.

Appendix A

In order to show the convergence of the algorithm some representative experimental results on various IBSR and BrainWeb MRI datasets are shown here in this Appendix. In Table 11 typical summary of the differences in cluster centers in between two successive iterations are shown. From the table it is observed experimentally that as the iterations progress the difference between the cluster centers in two successive iterations goes on decreasing and finally after certain iterations the differences goes down a predefined small threshold value (usually 0.001)and algorithms converges, indicating the fact that the pixels (re)partitioning process is over. Please note that in all the experiments the datasets pixel values [0 to 255] are normalized with in a range [0 to 1]. The plots of differences in cluster centers in two successive iterations performed on different IBSR and BrainWeb MRI datasets are also shown in Fig. 17 to represent the convergence of the algorithm. From the figures it is observed that in most of the datasets the algorithm finally converges when the difference in cluster centers (asymptotically) reaches the value close to zero. Once converged, the confusion matrices shown in Tables 12–15 obtained by the proposed method for different datasets (viz., IBSR 144, IBSR 155, BrainWeb Z85, and BrainWeb Z100 respectively) become diagonally dominant (by rows and by columns) which agrees well with the theory of Gauss-Seidel method for convergence of any iterative algorithm.

Table 11
Summary of the differences in cluster centers in between two successive iterations performed on various IBSR and BrainWeb brain MRI datasets.

Successive iterations	Difference in cluster centers			
	IBSR 144	IBSR 155	Z85	Z100
0 and 1	0.0632	0.0967	0.1362	0.1770
1 and 2	0.0302	0.0850	0.0800	0.0828
2 and 3	0.0192	0.0587	0.0531	0.0677
3 and 4	0.0124	0.0475	0.0473	0.0639
4 and 5	0.0090	0.0335	0.0372	0.0546
5 and 6	0.0056	0.0212	0.0310	0.0258
6 and 7	0.0042	0.0142	0.0271	0.0278
7 and 8	0.0029	0.0086	0.0077	0.0373
8 and 9	0.0020	0.0069	0.0038	0.0162
9 and 10	0.0011	0.0050	0.0017	0.0064
10 and 11	9.0460e − 04	0.0047	0.0010	0.0031
11 and 12	Converged	0.0026	7.1220e − 04	0.0014
12 and 13		0.0026	Converged	0.0011
13 and 14		0.0019		6.0120e − 04
14 and 15		0.0010		Converged
15 and 16		5.8356e − 04		
16 and 17		Converged		

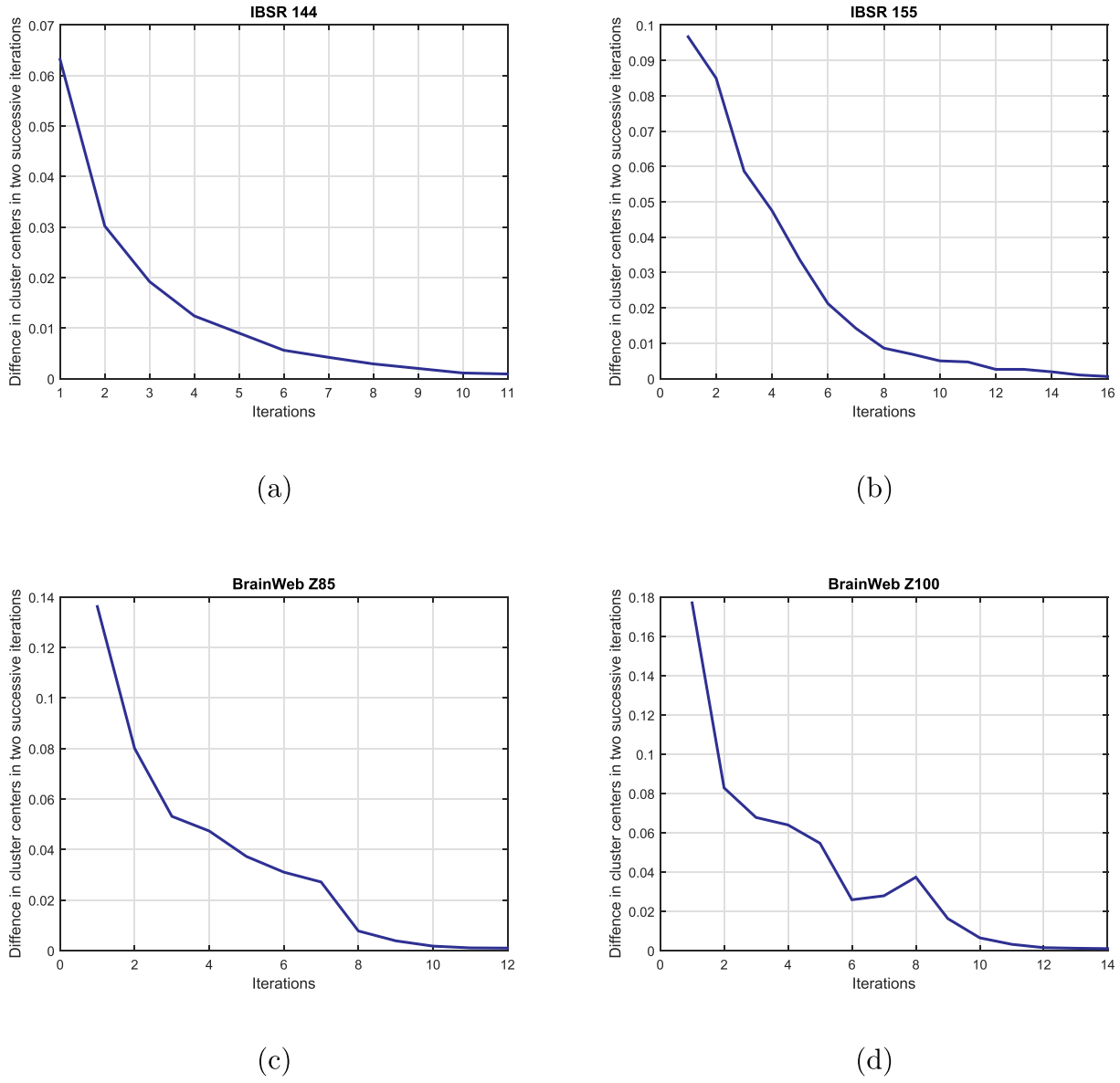

Fig. 17. Plots of differences in cluster centers in two successive iterations performed on different IBSR and BrainWeb MRI datasets.

Table 12
Confusion matrices of the segmented image performed on IBSR 144 brain MRI datasets.

Estimated segment	True segment			
	BG	CSF	GM	WM
BG	19443	0	35	0
CSF	62	904	93	0
GM	143	1172	5114	876
WM	2	43	410	4471

Table 13
Confusion matrices of the segmented image performed on IBSR 155 brain MRI datasets.

Estimated segment	True segment			
	BG	CSF	GM	WM
BG	19,980	0	0	0
CSF	35	647	4	0

(*continued on next page*)

Table 13 (*continued*)

Estimated segment	True segment			
	BG	CSF	GM	WM
GM	13	890	4339	82
WM	0	47	525	6206

Table 14
Confusion matrices of the segmented image performed on BrainWeb Z85 brain MRI datasets.

Estimated segment	True segment			
	BG	CSF	GM	WM
BG	19,669	77	44	0
CSF	114	2574	32	0
GM	0	508	7006	1264
WM	104	0	128	7757

Table 15
Confusion matrices of the segmented image performed on BrainWeb Z100 brain MRI datasets.

Estimated segment	True segment			
	BG	CSF	GM	WM
BG	21,316	7	14	1
CSF	14	2082	24	0
GM	0	413	4395	1756
WM	0	0	19	9236

References

[1] Haidekker M A. Medical imaging technology. 1st ed. New York: Springer; 2013.
[2] Balafar M A, Ramli A R, Saripan M I, Mashohor S. Review of brain MRI image segmentation methods. Artif Intell Rev 2010;33(4):261–74.
[3] Suetens P. Fundamentals of medical imaging. 1st ed. Cambridge, UK: Cambridge University Press; 2002.
[4] Maji P, Pal S K. Rough-fuzzy Pattern recognition: applications in bioinformatics and medical imaging. New Jersey and Canada: John Wiley & Sons, Inc; 2012.
[5] Bauer S, Wiest R, Nolte L P, Reyes M. A survey of MRI based medical image analysis for brain tumor studies. Phys Med Biol 2013;58(13):97–129.
[6] Bishop C M. Pattern recognition and machine learning (information science and statistics). 1st ed. Verlag New York: Springer; 2006.
[7] Gonzalez R C, Woods R E. Digital image processing. 3rd ed. India: Pearson; 2017.
[8] Theodoridis S, Koutroumbas K. Pattern recognition. 4th ed. New York: Academic Press; 2009.
[9] Manousakes I N, Undrill P E, Cameron G G. Split and merge segmentation of magnetic resonance medical images: performance evaluation and extension to three dimensions. Comp Biomed Res 1998;31(6):393–412.
[10] Subudhi B N, Thangaraj V, Sankaralingam E, Ghosh A. Tumor or abnormality identification from magnetic resonance images using statistical region fusion based segmentation. Magn Reson Imaging 2016;34(9):1292–304.
[11] Banerjee S, Mitra S, Umashankar B. Single seed delineation of brain tumor using multi-thresholding. Inf Sci 2016;330(4):88–103.
[12] Rajapakse J C, Giedd J N, Rapoport J L. Statistical approach to segmentation of single channel cerebral MR images. IEEE Trans Med Imaging 1997;16(2):176–86.
[13] Singleton H R, Pohost G M. Automatic cardiac MR image segmentation using edge detection by tissue classification in pixel neighborhoods. Magn Reson Med 1997;37(3):418–24.
[14] Banerjee A, Maji P. Rough-probabilistic clustering and hidden Markov random field model for segmentation of HEp-2 cell and brain MR images. Appl Soft Comput 2016;46(C):558–76.
[15] Saha S, Bandyopadhyay S. MRI brain image segmentation by fuzzy symmetry based genetic clustering technique. Proceedings of the IEEE Congress on Evolutionary Computation (CEC). 2007. p. 4417–24.
[16] Maji P, Roy S. Rough-fuzzy clustering and unsupervised feature selection for wavelet based MR image segmentation. PLoS One 2015;10(4):1–30.
[17] Vishnuvarthanana G, Rajasekaran M P, Subbaraj P, Vishnuvarthanan A. An unsupervised learning method with a clustering approach for tumor identification and tissue segmentation in magnetic resonance brain images. Appl Soft Comput 2016;38(C):190–212.
[18] Sarkara J P, Saha I, Maulik U. Rough possibilistic type-2 fuzzy c-means clustering for MR brain image segmentation. Appl Soft Comput 2016;46(C):527–36.
[19] Ravishankar S, Bresler Y. MR image reconstruction from highly under sampled k-space data by dictionary learning. IEEE Trans Med Imaging 2011;30(5):1028–41.
[20] Dahshan E S A E, Mohsen H M, Revett K, Salem A B M. Computer-aided diagnosis of human brain tumor through MRI: a survey and a new algorithm. Exp Syst Appl 2014;41(11):5526–45.
[21] Liu J, Li M, Wang J, Wu F, Liu T, Pan Y. A survey of MRI based brain tumor segmentation methods. Tsinghua Sci Technol 2014;19(6):578–95.
[22] Gordillo N, Montseny E, Sobrevilla P. State of the art survey on MRI brain tumor segmentation. Magn Reson Imaging 2013;31(8):1426–38.
[23] Liu W, Lin W. Additive white gaussian noise level estimation in SVD domain for images. IEEE Trans Image Process 2013;3(22):872–83.
[24] Cattin P. Image restoration: introduction to signal and image processing. MIAC, University of Basel; 2013.
[25] Nowak R. Wavelet based rician noise removal for magnetic resonance imaging. IEEE Trans Image Process 1999;10(8):1408–19.
[26] Gudbjartsson H, Patz S. The rician distribution of noisy MRI dat. Magn Reson Med 1995;6(34):910–4.
[27] Healey G, Kondepudy R. Radiometric CCD camera calibration and noise estimation. IEEE Trans Pattern Anal Mach Intell 1994;16(3):267–76.
[28] Boncelet C. Handbook of image and video processing. Academic Press; 2005.
[29] Gonzalez R C, Woods R E. Digital image processing. 3rd ed. Pearson Prentice Hall; 2007.
[30] Meyer C R, Bland P H, Pipe J. Retrospective correction of intensity inhomogeneities in MRI. IEEE Trans Med Imaging 1995;14(1):36–41.
[31] Wells W M III, Grimson W E L, Kikinis R, Jolesz F A. Adaptive segmentation of MRI data. IEEE Trans Med Imaging 1996;15(4):429–42.
[32] Ahmed M N, Yamany S M, Mohamed N, Farag A A, Moriarty T. A modified fuzzy c-means algorithm for bias field estimation and segmentation of MRI data. IEEE Trans Med Imaging 2002;21(3):193–9.
[33] Liew A W C, Yan H. An adaptive spatial fuzzy clustering algorithm for 3-d MR image segmentation. IEEE Trans Med Imaging 2003;22(9):1063–75.
[34] Mitra S. Satellite image segmentation with shadowed c-means. Inf Sci 2011;181(3):3601–13.
[35] Hou Z. A review on MR image intensity inhomogeneity correction. Int J Biomed Imaging 2006:1–11. https://doi.org/10.1155/IJBI/2006/49515.
[36] Zadeh L A. Fuzzy sets. Inf Control 1965;8(3):338–53.
[37] Pawlak Z. Rough sets. Int J Comput Inf Sci 1982;11(5):341–56.
[38] Pawlak Z. Rough sets: theoretical aspects of reasoning about data. Dordrecht, Netherlands: Kluwer; 1991.

[39] Taylor J S, Cristianini N. Kernel method for pattern analysis. Cambridge University Press; 2004.
[40] Lingras P. Unsupervised rough set classification using gas. Intell Inf Syst 2001;12(3):215–28.
[41] Scholkopf B, Smol A J. Learning with kernels. Cambridge: MIT Press; 2002.
[42] Halder A. Kernel based rough fuzzy c-means clustering optimized using particle swarm optimization. Proceedings of the International Symposium on Advanced Computing and Communication (ISACC). 2015. p. 41–8.
[43] Hofmann T, Schölkopf B, Smola A J. Kernel methods in machine learning. Ann Stat 2008;36(3):1171–220.
[44] Barrett R, Berry M, Chan T, Demmel J, Donato J, Dongarra J. Templates for the solution of linear systems: building blocks for iterative methods. 2nd ed. Philadelphia, PA: SIAM; 1994.
[45] Maji P, Pal S K. Rough set based generalized fuzzy c-means algorithm and quantitative indices. IEEE Trans Syst Man Cybern B Cybern 2007;37(6):1529–40.
[46] Yan H. Convergence condition and efficient implementation of the fuzzy curve-tracing FCT algorithm. IEEE Trans Syst Man Cybern B Cybern 2004;34(1):210–21.
[47] Collins D L, Zijdenbos A P, Kollokian V, Sled J G, Kabani N J, Holmes C J, et al. Design and construction of a realistic digital brain phantom. IEEE Trans Med Imaging 1998;17(3):463–8.
[48] Rohlfing T. Image similarity and tissue overlaps as surrogates for image registration accuracy: widely used but unreliable. IEEE Trans. Med Imaging 2012;31(2):153–63.
[49] Li C L, Goldgof D B, Hall L O. Knowledge-based classification and tissue labeling of MR images of human brain. IEEE Trans Med Imaging 1993;12(4):740–50.
[50] Hall L O, Bensaid A M, Clarke L P, Velthuizen R P, Silbiger M S, Bezdek J C. A comparison of neural network and fuzzy clustering techniques in segmenting magnetic resonance images of the brain. IEEE Trans Neural Netw 1993;3(5):672–82.
[51] Maji P, Pal S K. RFCM: a hybrid clustering algorithm using rough and fuzzy sets. Fund Inform 2007;80(4):475–96.
[52] Chen S, Zhang D. Robust image segmentation using FCM with spatial constraints based on new kernel-induced distance measure. IEEE Trans Syst Man Cybern B Cybern 2004;34(4):193–9.
[53] Chen L, Zou J, Chen C L P. Kernel spatial shadowed c-means for image segmentation. Int J Fuzzy Syst 2014;16(1):46–56.
[54] Han J, Kamber M, Pei J. Data mining: concepts and techniques. 3rd ed. 2011.
[55] Congalton R, Green K. Assessing the accuracy of remotely sensed data: principles and practices. 1st ed. CRC Press; 2008.
[56] Das S, Sil S. Kernel-induced fuzzy clustering of image pixels with an improved differential evolution algorithm. Inf Sci 2010;180(8):1237–56.
[57] Tukey J W. Exploratory data analysis. Addison-Wesley; 1977.
[58] Rice J A. Mathematical statistics and data analysis. Advanced series Cengage Learning; 2006.